Building and Environment 154 (2019) 263–280

Contents lists available at ScienceDirect

Building and Environment

journal homepage: www.elsevier.com/locate/buildenv

# Cross-ventilation in a generic isolated building equipped with louvers: Wind-tunnel experiments and CFD simulations

Katarina Kosutova[a,*], Twan van Hooff[a,b], Christina Vanderwel[c], Bert Blocken[a,b], Jan Hensen[a]

[a] Department of the Built Environment, Eindhoven University of Technology, P.O. Box 513, 5600, MB Eindhoven, the Netherlands
[b] Department of Civil Engineering, KU Leuven, Kasteelpark Arenberg 40 - Bus 2447, 3001 Leuven, Belgium
[c] Aerodynamics and Flight Mechanics Research Group, University of Southampton, Bldg 13, Highfield Campus, SO16 7DY, Southampton, United Kingdom

ARTICLE INFO

*Keywords:*
Wind-tunnel experiments
Natural cross-ventilation
Ventilative cooling
Ventilation louvers
Numerical simulations
Air exchange efficiency

ABSTRACT

Natural ventilation can be used to improve indoor air quality, remove contaminants from spaces and to remove heat from a building during the day, or during the night. In some cases, openings for natural ventilation are equipped with shading devices – such as louvers – to reduce solar heat gains while allowing natural ventilation. This study presents wind-tunnel experiments and computational fluid dynamics (CFD) simulations of a cross-ventilated building equipped with louvers. Four opening positions are studied: (i) openings in the center, (ii) upper or (iii) lower part of the windward and leeward facades or (iv) one opening in the upper part of the windward facade and one opening in the lower part of the leeward facade. The 3D steady Reynolds-averaged Navier-Stokes (RANS) simulations are performed with three turbulence models (RNG k-ε, SST k-ω, RSM) and validated with the wind-tunnel experiments. The experimental results show that the largest velocities occur in a building with openings in the upper part of the facade. The best agreement with experimental data is provided by RSM. In addition, CFD simulations for buildings without louvers are conducted for the same opening positions to evaluate the effect of louvers on the dimensionless volume flow rate, age of air and air exchange efficiency. The highest dimensionless volume flow rate at reduced scale (0.69) is obtained in the building with louvered openings in the upper part of the facade and the highest air exchange efficiency is achieved for a building with louvered openings in the center of the facade (45%).

## 1. Introduction

Natural cross-ventilation is a commonly used technique to maintain a comfortable indoor environment and to remove pollutants (e.g. refs. [1–4]). In addition, it can be used as a passive cooling technique to reduce the cooling demand of buildings (e.g. refs. [5–7]). However, the performance of natural ventilation is heavily influenced by the design of the facade openings, such as windows. Moreover, practical concerns, such as prevention against rain, burglary or excessive solar radiation have to be addressed. Using architectural louvers can be an efficient solution as these can reduce the entrance of direct solar radiation (especially when they are opaque) and prevent rain penetration. However, louvers can have an impact on the amount of airflow penetrating through the openings [8] as well.

Several studies investigated single-sided ventilation [8,9] or cross-ventilation [10,11] through architectural louver systems. Chandrashekran [10] performed wind-tunnel experiments and computational fluid dynamics (CFD) simulations of cross-ventilation in an isolated building equipped with louvers. The author considered four different slat angles (0°, 15°, 30°, and 45°) and concluded that using louvers with angles of 0°, 15° and 30° results in higher indoor velocities in the central part of the building compared to other areas of the building. Louvers with a slat angle of 45° affect the flow direction and mainly result in high velocities close to the window inlet. This conclusion is in contradiction with the findings in the study by Tablada et al. [11], who used exterior louvers as a passive cooling strategy to improve thermal comfort inside a residential building in Sicily (Italy). For this purpose, the authors coupled CFD simulations with building energy simulations (BES) to investigate the effect of louvers with two slat angles: 0° and 45°. They concluded that louvers with a 0° slat angle have a negligible influence on the indoor airflow. However, in case of louvers with a 45° slat angle, velocities are reduced close to the window inlet and outlet. In addition, the conditions for thermal comfort were satisfied in 90–91% of the time period analyzed when using louvers in combination with natural ventilation. Differences in conclusions from these studies can arise from different building and window opening geometry or

* Corresponding author.
*E-mail address:* k.kosutova@tue.nl (K. Kosutova).

https://doi.org/10.1016/j.buildenv.2019.03.019
Received 7 October 2018; Received in revised form 9 March 2019; Accepted 11 March 2019
Available online 15 March 2019

**Nomenclature**

*Roman symbols*

| | |
|---|---|
| $\|V\|$ | Mean velocity magnitude, [m/s] |
| $A_w$ | Opening area, [$m^2$] |
| $C_\mu$ | Empirical constant, [−] |
| $F_s$ | Safety factor, [−] |
| H | Height of the building, [m] |
| I | Turbulence intensity, [%] |
| k | Turbulent kinetic energy, [$m^2/s^2$] |
| O | Observed value of mean velocity, [m/s] |
| P | Predicted value of mean velocity, [m/s] |
| p | Formal order of accuracy, [−] |
| Q | Volume flow rate, [$m^3/s$] |
| $r^p$ | Linear grid refinement factor, [−] |
| U | Streamwise mean velocity, [m/s] |
| u | Instantaneous velocity component in x direction |
| $u^*_{ABL}$ | Atmospheric boundary layer friction velocity, [m/s] |
| $U_{BASIC}$ | Mean velocity obtained on basic grid, [m/s] |
| $U_{FINE}$ | Mean velocity obtained on fine grid, [m/s] |
| $U_{ref}$ | Reference velocity, [m/s] |
| v | Instantaneous velocity component in y direction |
| w | Instantaneous velocity component in z direction |
| x | Horizontal coordinate, [m] |
| y | Vertical coordinate, [m] |
| $y_0$ | Aerodynamic roughness length, [m] |

*Greek symbols*

| | |
|---|---|
| ε | Turbulence dissipation rate, [$m^2/s^3$] |
| $\varepsilon_A$ | Air exchange efficiency, [%] |
| σ | Standard deviation of turbulent fluctuations, [m/s] |
| τ | Age of air, [s] |
| $\nu$ | Kinematic viscosity [$m^2/s$] |
| ω | Specific dissipation rate, [1/s] |

*Acronyms*

| | |
|---|---|
| ABL | Atmospheric boundary layer |
| CCD | Couple charged camera |
| CFD | Computational fluid dynamics |
| FAC1.3 | Factor of 1.3 observations |
| FAC2 | Factor of two observations |
| FB | Fractional bias |
| GCI | Grid convergence index |
| NMSE | Normalized mean square error |
| PIV | Particle image velocimetry |
| PMMA | Polymethyl methacrylate |
| RANS | Reynolds averaged Navier-Stokes |
| RNG | Renormalization group |
| RSM | Reynolds stress model |
| SIMPLE | Semi implicit method for pressure linked equations |
| SST | Stress-shear transport |

*Dimensionless numbers*

| | |
|---|---|
| Re | Reynolds number |

from differences in the computational grid and other computational settings and/or boundary conditions. The aforementioned studies investigated natural ventilation in a building equipped with louvers for one opening position. However, the opening position can have a strong influence on the indoor airflow, air change rates and also on pollutant dispersion (e.g. refs. [12–18]). In the past, several studies focused on assessing the influence of the opening position on natural ventilation either by experiments (e.g. refs. [12,13]) or by numerical simulations (e.g. refs. [14–18]). Although these studies were carried out for plain openings (without louvers or other obstructions), they do provide interesting information regarding the indoor airflow pattern in a cross-ventilated building as function of opening location. Karava et al. [12] performed wind-tunnel experiments for nine different opening positions in a generic isolated building and demonstrated that the opening position influences the air velocity and the airflow pattern inside the building as well as the airflow rates through the building. The airflow rate through the building with openings in the lower part of the facade was lower than that obtained in a building with openings in the center or upper part of the facade. These conclusions are in line with the results from the study by Tominaga and Blocken [13], who performed wind-tunnel experiments for a geometrically similar building. The authors reported the highest airflow rate for the building with openings in the upper part of the building, while the lowest airflow rate was measured in the building with one opening at the bottom of the windward facade and one opening at the upper part of the leeward facade. Furthermore, they concluded that recirculation regions and concentration fields are mostly influenced by position of the inlet (windward) opening [13].

Numerical studies on natural cross-ventilation flows in buildings are often performed using CFD (e.g. refs. [18–28]), since these airflows can be considered challenging due to the interaction between indoor airflow and outdoor wind flow, especially in buildings with large openings (e.g. ref. [14]). However, CFD simulations are very sensitive to the chosen approach, turbulence model, boundary conditions, etc. (e.g refs. [14,16,19–21]). For example, Ramponi and Blocken [14] showed the impact of numerical and physical diffusion on the results of CFD simulations of cross-ventilation flows. They conducted 3D steady RANS simulations and compared the results with the wind-tunnel experiments by Karava et al. [12] for a generic building with large and small openings and for two opening positions (openings in the center and bottom of the facade). The authors found that the effect of numerical (artificial) and physical diffusion was very similar and was most pronounced inside the building. A substantial amount of numerical diffusion was attributed to the use of low-resolution grids and the use of first-order schemes, therefore the authors recommended using at least second-order discretization schemes and high-resolution computational grids. Considering the choice for a turbulence model for CFD simulations of natural cross-ventilation, conclusions from different studies are often contradictory. For example, van Hooff et al. [19] performed CFD simulations of cross-ventilation flows in a generic building and concluded that the standard k-ε model provided the best agreement with the experimental data by Tominaga and Blocken [13], while the worst agreement was obtained by the realizable k-ε model and the employed Reynolds stress model (RSM). Ramponi and Blocken [20] concluded in their validation study that the best agreement with experimental data was obtained by the shear-stress transport (SST) k-ω model. Hu et al. [22] found that the standard k-ω and SST k-ω models provided a very good agreement with experiments, while the renormalization group (RNG) k-ε model and the standard k-ε model failed to predict the main characteristics of the flow close to the openings. Lee et al. [29]. compared CFD simulations with the particle image velocimetry (PIV) experiments conducted for a generic greenhouse and concluded that the most accurate results were obtained by the RNG k-ε model and RSM. Note that the studies mentioned above (i.e. [12–29]) were all

performed for window openings without louvers.

This study presents wind-tunnel experiments and CFD simulations of natural cross-ventilation in a generic isolated cubic building equipped with louvers for four different window opening positions. Both wind-tunnel experiments and the CFD simulations are carried out under isothermal conditions. The objective of the study is threefold. First, to validate 3D steady RANS CFD simulations – in combination with three different turbulence models: RNG k-ε, SST k-ω and RSM – using new wind-tunnel experiments. Second, to investigate the impact of louvers and different opening positions on the indoor airflow pattern and indoor velocities by means of both experimental data and CFD simulations. Third, to investigate the impact of window opening positions on the airflow pattern, age of air, dimensionless volume flow rate and air exchange efficiency in a building equipped with louvers. To the best knowledge of the authors, a study combining wind-tunnel experiments and CFD simulations to investigate the impact of the position of window openings equipped with louvers on indoor airflow and air exchange efficiency has not yet been performed. The wind-tunnel experiments are described in Section 2. Section 3 reports the CFD simulations of the reference case including a systematic grid-sensitivity analysis. The performance of the three RANS turbulence models for each opening position is evaluated in Section 4. Section 5 describes the influence of the opening position on the dimensionless volume flow rate and air exchange efficiency. Section 6 (Discussion) and Section 7 (Conclusion) conclude the paper.

## 2. Experimental model

The wind-tunnel experiments are performed for a single-zone cubic building model with dimensions $0.15 \times 0.15 \times 0.15\,m^3$ (scale 1:50). This scale is based on the blockage ratio in the wind tunnel and dynamic similarity criteria. The building has one opening at the windward and one opening at the leeward facade, both with a size of $0.07 \times 0.04\,m^2$, yielding a facade porosity of 12.5%. The building model is constructed using 0.01 m thick polymethyl methacrylate (PMMA) sheets connected by plastic bolts. The wind-tunnel experiments are performed for four different opening positions: openings in the center of the facade (Fig. 1a, Fig. 2a), i.e. configuration “Center”, openings at the bottom part of the facade (Figs. 1b and 2b), i.e. configuration “Down”, openings at the upper part of the facade (Figs. 1c and 2c), i.e. configuration “Up”, and a windward opening at the upper part and a leeward opening at the lower part of the facade (Figs. 1d and 2a,c), i.e. configuration “UpDown”. In all four configurations both openings are equipped with ventilation louvers with three slats with a 15° angle (Fig. 3a–b). This particular slat angle is chosen because it provides enough free area (i.e. the space between the two louver slats) for the air to pass through and provide cross-ventilation while also providing some shading. Configurations with larger louver slat angles (30° or 45°) would result in a smaller free area and therefore less air entering the building. The louver slat angle is an important parameter as the resulting free area has an influence on the pressure difference across the window, indoor air velocities and indoor airflow pattern. Moreover, the choice of the louver slat angle was restricted by the size of the opening of the experimental model. The ventilation louvers are made of 0.75 mm thick polypropylene sheet. First, a frame is constructed out of polypropylene sheet, consequently the louver slats are glued to the vertical sides of the frame and the whole construction is inserted in the windward and leeward opening of the building.

## 3. Experimental setup

### 3.1. Wind-tunnel setup

An open-circuit wind tunnel at the University of Southampton is used to perform the experiments [30,31]. The test section of the wind tunnel is 0.6 m high, 0.9 m wide and 4.5 m long. Four spires with a height 0.427 m, three types of roughness blocks with decreasing height (32 mm, 16 mm and 7 mm) and a 0.3 m long strip of carpet are used to create a neutral atmospheric boundary layer (ABL) approach flow characterized by an ABL friction velocity of $u^*_{ABL} = 0.195$ m/s and a reduced-scale aerodynamic roughness length of $y_0 = 0.0024$ m (0.12 m in full scale corresponding to roughly open terrain according to the Davenport-Wieringa roughness classification [32,33]). The incident vertical profile of the streamwise mean velocity obtained by PIV measurements in the empty test section is shown in Fig. 4a and follows the logarithmic equation:

$$U = \frac{u^*_{ABL}}{\kappa} \cdot ln\frac{y}{y_0} \tag{1}$$

where κ is the von Karman constant equal to 0.42.

The turbulence intensity for streamwise ($I_u$) and vertical ($I_v$) direction (Fig. 4b) is given by Eq. (2):

$$I_u = \frac{\sigma_u}{U_{ref}}, \quad I_v = \frac{\sigma_v}{U_{ref}} \tag{2}$$

where $\sigma_u$ and $\sigma_v$ are the turbulent fluctuations in streamwise and vertical direction, respectively, and $U_{ref}$ is the streamwise mean velocity at $y = 0.15$ m (building height) equal to 1.9 m/s. The turbulence intensity

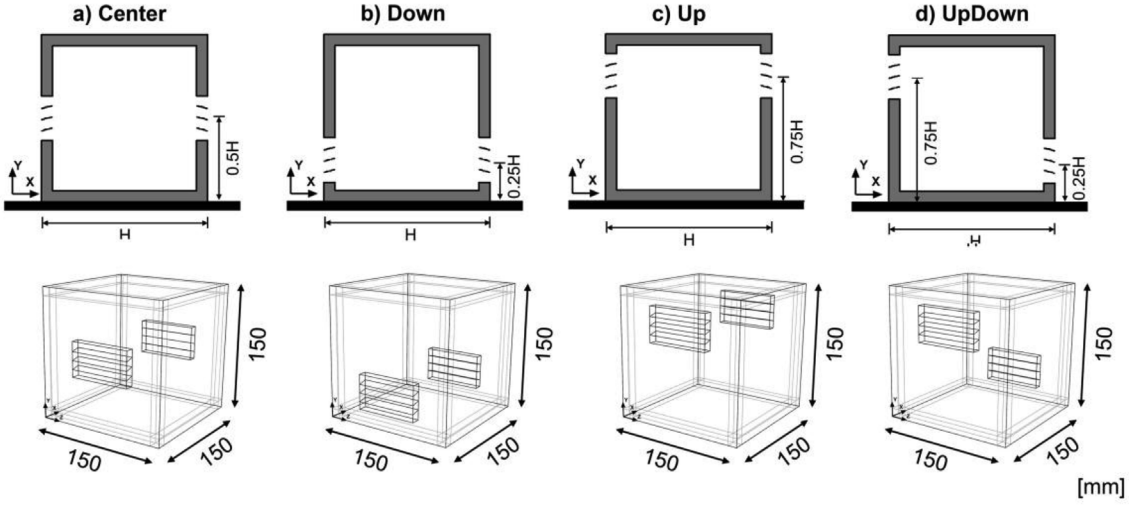


**Fig. 1.** Geometry of the reduced-scale building models used for the experiments: (a) configuration “Center”, (b) configuration “Down”, (c) configuration “Up” and (d) configuration “UpDown”. All dimensions are in mm.

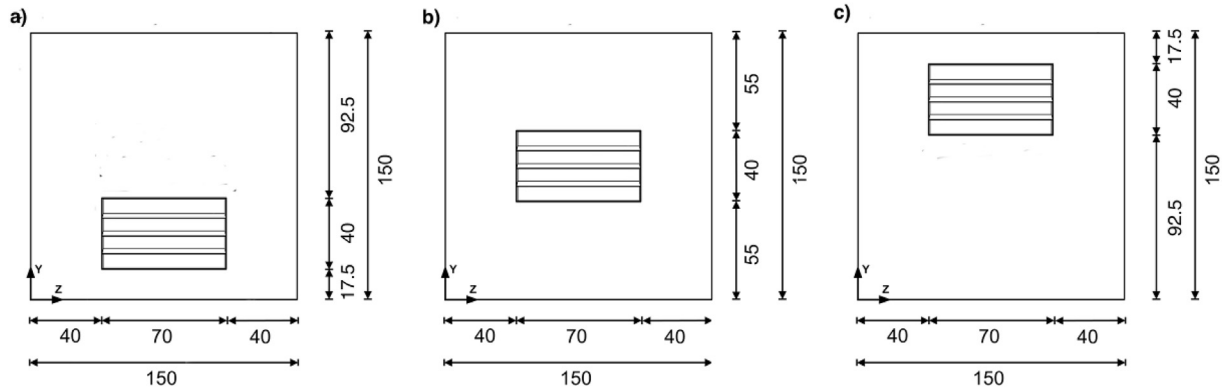


**Fig. 2.** Details of the windward/leeward facade of the building model with the opening at three different locations. Dimensions are in mm.

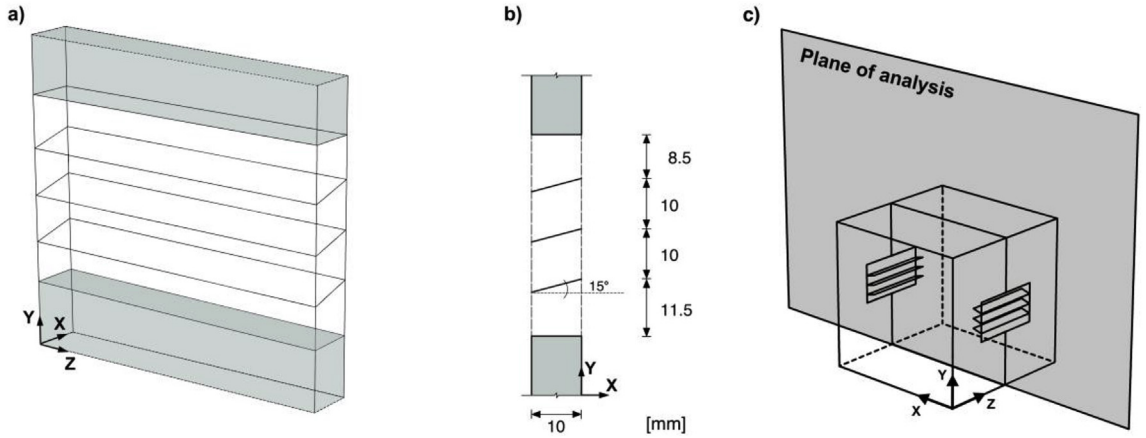


**Fig. 3.** (a) Detail of the ventilation louver, (b) cross-section of the ventilation louver. (c) Plane of analysis.

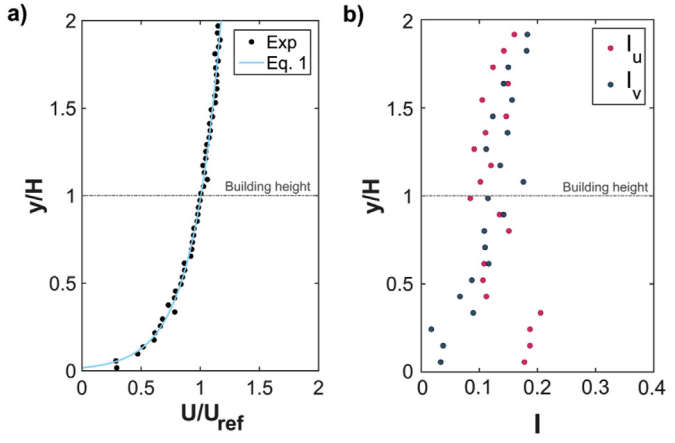


**Fig. 4.** (a) Incident profile of time-averaged streamwise velocity $U/U_{ref}$ and (b) turbulence intensity in streamwise ($I_u$) and vertical ($I_v$) direction.

in streamwise direction is about 10% at the building height.

The roughness setup is based on the previous work by Taddei et al. [30]. The experimental setup including the PIV setup is shown in Fig. 5a, the roughness setup is depicted in Fig. 5b and a schematic of the PIV setup is shown in Fig. 5c.

### 3.2. Velocity measurements

The 2D PIV measurements are carried out in the vertical centerplane for all four configurations (Fig. 5c). A laser sheet is created using two double pulse Nd:YAG lasers (Nano L200 15PIV, Litron Lasers), a set of mirrors and spherical lenses (Fig. 5c). The flow is seeded by smoke created from a solution of glycol and demineralized water. A charged coupled device (CCD) camera (VC-Imager Pro Lx 16 M) with AF Nikkor 50 mm f/1.8D lens positioned normal to the flow direction is used to capture the particle images. Measurements are acquired at a rate of 0.7 Hz and 500 statistically independent vector fields are obtained for each measurement set, allowing a correct evaluation of turbulence fluctuations and scales and an accurate statistical analysis of mean and turbulent characteristics of the flow. The results are post-processed in DaVis 8.2.0 software using an interrogation window size of 32 × 32 pixels and 50% overlap. The PIV measurements are carried out using the guidelines by Prasad [34]. The PIV measurements are conducted for a wind direction perpendicular to the facades with openings and a reference streamwise velocity ($U_{ref}$) of 1.9 m/s at building height (H = 0.15 m) corresponding to a building Reynolds number of 19,000 (Eq. (3)).

$$Re = \frac{U_{ref} H}{\nu} \tag{3}$$

with $\nu = 1.56 \times 10^{-5}$ m$^2$/s the kinematic viscosity of air at 25.5 °C.

### 3.3. Results

The PIV measurement results in terms of time-averaged velocity vector fields in the vertical centerplane (z/H = 0.5) are shown in Fig. 6a–d. In all four configurations the flow is dominated by the jet passing between the windward and leeward opening. Fig. 6a shows the mean velocity vector field for configuration “Center”. The jet passing through the windward opening is directed upwards under an angle of about 19° due to the louver slats, however, the jet hardly reaches the ceiling of the room. In the upper part close to the leeward opening, a

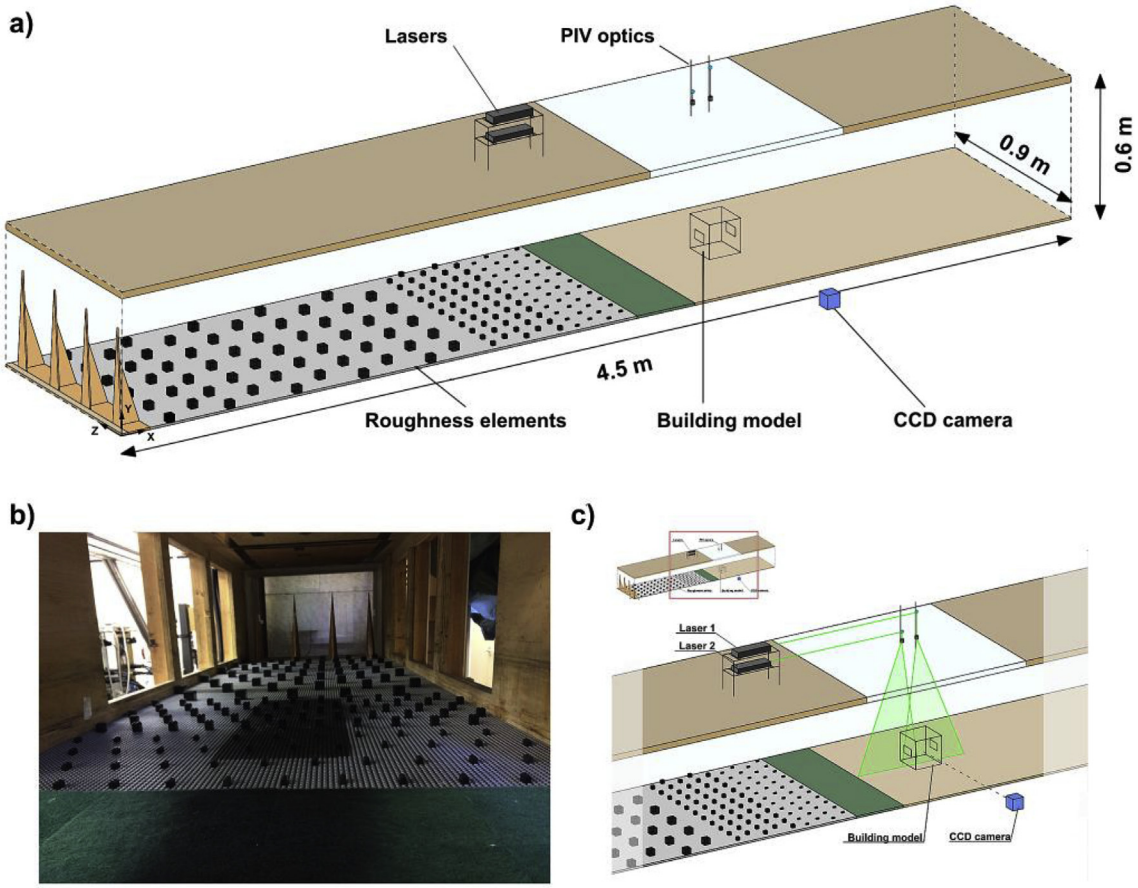


**Fig. 5.** (a) Setup of the wind tunnel used for the experiments, (b) roughness setup and (c) detail of the PIV setup.

small recirculation zone is formed, while a large low-velocity zone is present below the jet. The highest dimensionless streamwise mean velocity ($U/U_{ref} = 0.57$) is measured at the core of the jet entering through the windward opening. A standing vortex is present in front of the building. The mean velocity vector field for configuration "Down" is shown in Fig. 6b. The incoming jet is directed upwards under an angle of about 12° and it spreads throughout the lower part of the room, just above the floor. The largest dimensionless streamwise mean velocity ($U/U_{ref} = 0.53$) is measured at the core of the jet close to the windward opening. A large counter-clockwise recirculation zone is formed above the jet. Configuration "Up" is depicted in Fig. 6c. The jet attaches to the ceiling under an angle of about 17°, while below the jet, a large low velocity zone is formed with air circulating in a clock-wise direction. The maximum dimensionless streamwise mean velocity of $U/U_{ref} = 0.76$ is measured in the middle of the centerplane close to the ceiling. This velocity is 25% and 30% higher than the maximum velocity measured for configurations "Center" and "Down", respectively. Fig. 6d shows the configuration "UpDown". In this case, the jet attaches to the ceiling under an angle of about 14° and forms a downward directed wall jet at the leeward facade of the room. A recirculation zone is formed below the ceiling jet. The maximum dimensionless streamwise mean velocity ($U/U_{ref} = 0.54$) is measured near the ceiling and it is 29% lower than the maximum value measured for the "Up" configuration. The highest measured velocities of the jet are present for the configuration "Up". This is caused by the combination of the upward direction of the jet caused by the louvers and the position of the openings close to the ceiling. Because of this combination, the jet is driven against the ceiling, which inhibits extensive jet spreading as in the other configurations. The movement of the jet along the ceiling provides the most direct route with minimal flow energy losses between inlet and outlet opening. In addition, the windward opening is located at the position where, with a closed building, the stagnation point would occur, which is the area of the highest pressure at the windward facade.

## 4. CFD simulation setup

### 4.1. Computational domain and grid

The computational geometry corresponds to the reduced-scale geometry used for the wind-tunnel experiments. The building walls, including floor and ceiling, with a thickness of 0.01 m are explicitly included in the computational building geometry. The louver slats are modeled as zero-thickness walls given their small thickness of 0.75 mm in the experiments. The computational domain for the CFD simulations is created following the best practice guidelines by Tominaga et al. [35], Franke et al. [36] and Blocken [37]. The upstream length of the domain is reduced to 3H (H = height of the building) to avoid unintended streamwise gradients in the approach-flow profiles [14,37,38]. The distance from the building to the lateral sides and to the top of the domain is 5H while the downstream length of the domain is 15H, resulting in domain dimensions of $1.65 \times 2.85 \times 0.9\,m^3$ (W × L × H) (Fig. 7a). The surface grid-extrusion technique proposed by van Hooff and Blocken [39] is used to create the computational grid, resulting in 942,270 hexahedral cells with increased spatial resolutions close to the sharp edges of the building, window openings and louver slats (Fig. 7b).

### 4.2. Boundary conditions and solver settings

The boundary conditions for the CFD simulations are chosen to reproduce the conditions during the wind-tunnel experiments as much as possible. A logarithmic mean wind speed profile is imposed at the

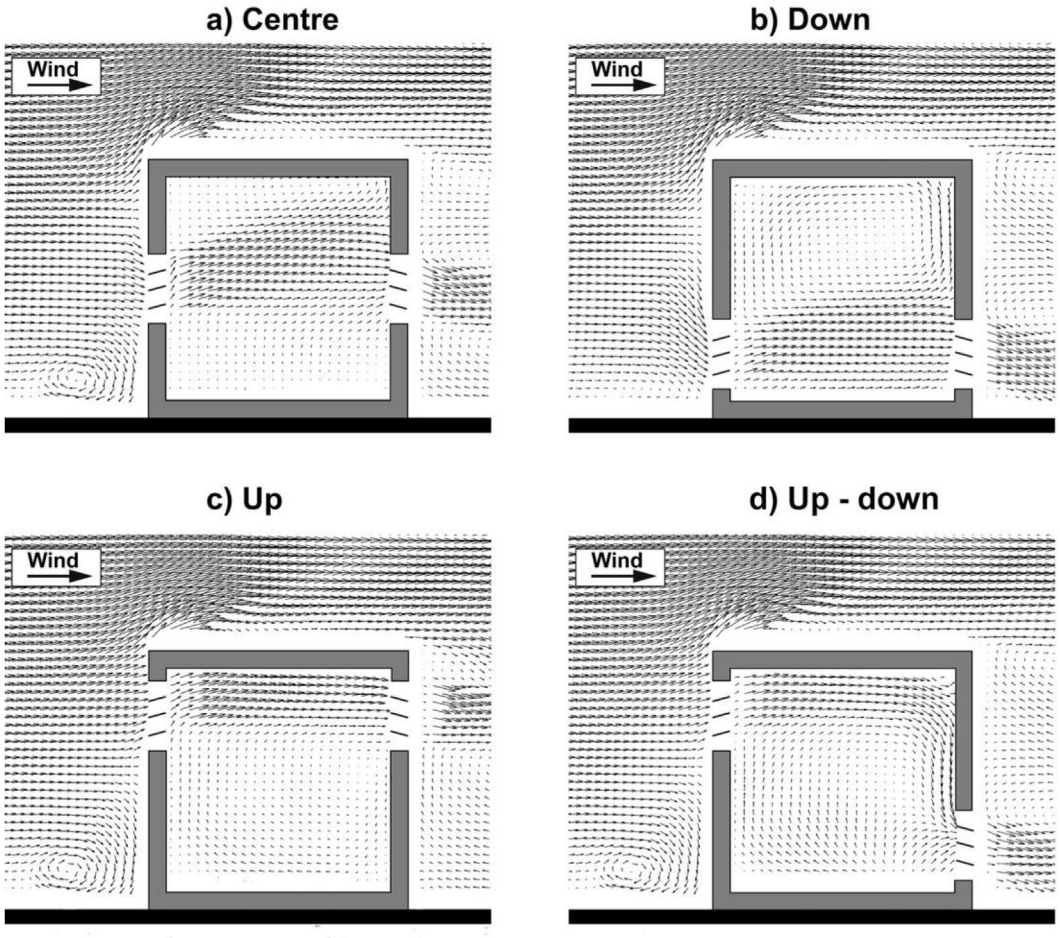


**Fig. 6.** Mean velocity vector field in the vertical centerplane obtained by PIV for all four configurations. (a) "Center"; (b) "Down"; (c) "Up"; (d) "UpDown".

inlet based on a fit with experimental data using Eq. (1). In order to obtain an inlet profile for turbulent kinetic energy, the standard deviations of the turbulent fluctuations in the three directions should be known (Eq. (4)).

$$k = \frac{1}{2}\cdot(\sigma_u^2 + \sigma_v^2 + \sigma_w^2) \tag{4}$$

Only two components are measured in the wind tunnel: $\sigma_u$ and $\sigma_v$, and the assumption $\sigma_u{}^2 \approx \sigma_v{}^2 + \sigma_w{}^2$ is therefore made to estimate $\sigma_w$ [35], yielding:

$$k = \frac{1}{2}\cdot(\sigma_u^2 + \sigma_v^2 + (\sigma_u^2 - \sigma_v^2)) = \sigma_u^2 \tag{5}$$

The turbulence dissipation rate is based on Eq. (6):

$$\varepsilon = \frac{u_{ABL}^{*3}}{\kappa(y + y_0)} \tag{6}$$

The specific dissipation rate for the SST k-ω model is given by Eq. (7):

$$\omega = \frac{\varepsilon}{C_\mu k} \tag{7}$$

where $C_\mu$ is an empirical constant equal to 0.09. Zero static gauge pressure is imposed at the outlet plane. Zero normal gradients and zero normal velocities are imposed at the top and lateral sides of the domain.

The 3D steady RANS approach is by far the most commonly used CFD approach in natural ventilation studies [40–42]. In the present study, 3D steady isothermal RANS simulations are performed with three different turbulence models: RNG k-ε [43,44] SST k-ω [45] and RSM

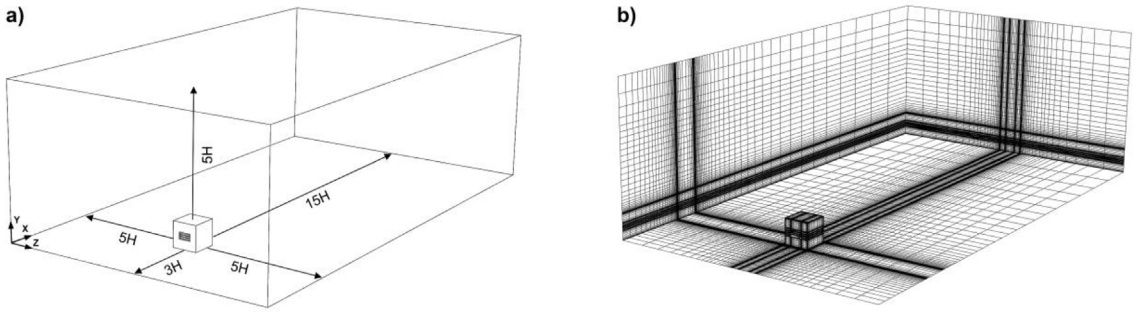


**Fig. 7.** (a) Computational domain with dimensions; H = 150 mm (reduced-scale building height), (b) grid on building and domain surfaces.

[46] using ANSYS Fluent 15.0. The two eddy-viscosity models, RNG k-ε and the SST k-ω, are chosen because they emerged as some of the best performing RANS turbulence models from earlier validation studies [16,20,26]. The RSM is chosen due to its potential to provide a better performance compared to eddy-viscosity models, since it solves transport equations for each of the six Reynolds stresses. In addition, it emerged as the best model along with RNG k-ε in the study conducted by Lee at al [29]. For the ground surface, either enhanced wall treatment is used for the RNG k-ε model and RSM, or an automated wall treatment for the SST k-ω model. Both enhanced and automated wall treatment allow the flow to be solved all the way down to the viscous sublayer for the fine grid close to the wall, while wall functions are used when the grid resolution close to the wall is insufficient [47]. The SIMPLE algorithm is used for pressure-velocity coupling. Second-order discretization schemes are used for convective and viscous terms of the governing equations and for pressure. The streamwise velocity is monitored in three points in order to assess the convergence of the solution. The scaled residuals reach a minimum of $10^{-4}$ for momentum, $10^{-5}$ for turbulent kinetic energy, $10^{-5}$ for turbulence dissipation rate and $10^{-5}$ for x-,y- and z-velocity.

A check of the horizontal homogeneity [37,38] of the vertical profile of the mean wind speed is performed in an empty domain for the RNG k-ε model (Fig. 8). The dimensionless streamwise inlet velocity ($U/U_{ref}$) profile is compared with the incident profile at the building location. A small acceleration near the ground is present in the incident profile, which is caused by the absence of ground roughness in the upstream part of the computational domain in order to resemble the smooth wind tunnel fetch directly upstream of the model (Fig. 5a). However, this acceleration is also observed in the wind tunnel when the air flows over the smooth part of the ground upstream of the building [13].

### 4.3. Grid-sensitivity analysis

A systematic grid-sensitivity analysis is conducted for configuration "Center" using the RNG k-ε turbulence model in combination with enhanced wall treatment. Three grids are subjected to the analysis: (a) coarse grid with 324,820 cells; (b) basic grid with 942,270 cells; and (c) fine grid with 2,648,972 cells. The basic grid is coarsened/refined by √2 in each direction to obtain the coarse and the fine grid. Fig. 9a–c shows the computational grids including a detail of the louver grid. The numbers of cells along the louver length are 14, 20 and 28 for the coarse, basic and fine grid, respectively. The cell count along the louver width is 7, 10, and 14 for coarse, basic and fine grid, respectively. The dimensionless wall distance ($y^*$) taken on the centerline of the ceiling inside the building in streamwise direction ranges from 5.4 to 11.4 for the coarse grid, 2.8 to 7.9 for the basic grid and 1.7 to 5.7 for the fine grid.

Fig. 10 presents the results from the grid-sensitivity analysis in terms of the dimensionless streamwise mean velocity ($U/U_{ref}$) along four vertical lines in the vertical centerplane at z/H = 0.5. The fine and the basic grid provide almost identical results along these lines. Some differences are present between the coarse and the basic grid. An estimate of the error of $U/U_{ref}$ on the basic grid is calculated using the grid-convergence index (GCI) proposed by Roache [48] (Eq. (8)).

$$GCI_{Basic} = F_s \left| \frac{r^p [(U_{Basic} - U_{Fine})/U_{ref}]}{1 - r^p} \right| \quad (8)$$

where $F_s$ is the safety factor with the recommended value of 1.25 when three or more grids are compared, $r^p$ is the linear grid refinement factor (√2) and p = 2 is the formal order of accuracy, based on the use of second-order discretization schemes for the simulations. The GCI estimates the error of the basic grid by comparing the velocities obtained with the basic grid with the velocities obtained with the fine grid. The values of the GCI averaged along each vertical line are 0.55% for x/L = 0.2, 2.07% for x/L = 0.4, 0.98% for x/L = 0.6 and 0.55% for x/L = 0.8 (Fig. 11). Based on these results, it can be concluded that the basic grid provides nearly grid-independent results and it is therefore used for the remainder of this study.

## 5. CFD simulations: validation

### 5.1. Mean velocity profiles

Fig. 12 shows a comparison of experimentally and numerically obtained values of the dimensionless streamwise mean velocity ($U/U_{ref}$) along four vertical lines in the vertical centerplane for configuration "Center". Note that above y/H = 0.95 the results are omitted since these are compromised by unwanted reflections of the laser sheet on the surface. Overall, the performance of the three turbulence models is quite similar. The effect of the individual louver slats is visible at x/H = 0.2, mostly in the experimental data and in the results predicted by the SST k-ω model, however, this effect vanishes further downstream. Note that this effect is similar to the merging of multiple confluent jets (e.g. Ref. [49]). The fact that this effect is most pronounced when using the SST k-ω model can be attributed to the lower levels of turbulent kinetic energy ($k/U_{ref}^2$) inside the building predicted by this model (Fig. 13b). The results obtained by RNG k-ε (Fig. 13a) and RSM (Fig. 13c) show higher levels of turbulent kinetic energy outside of the building, close to the upper part of the windward facade, which are

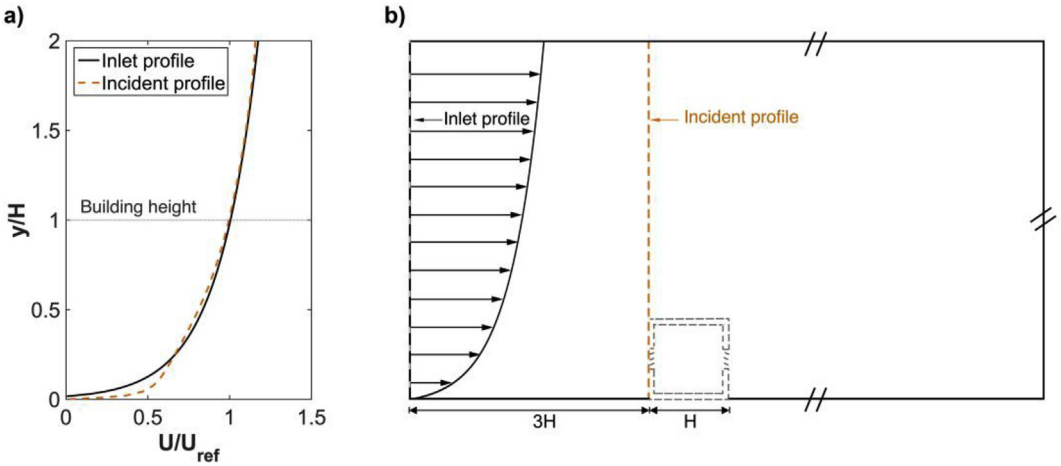


**Fig. 8.** (a) Comparison of inlet and incident profile of dimensionless streamwise mean velocity ($U/U_{ref}$); incident profile obtained using RNG k-ε turbulence model. (b) Schematic cross-section of the domain indicating the position of inlet and incident profiles.

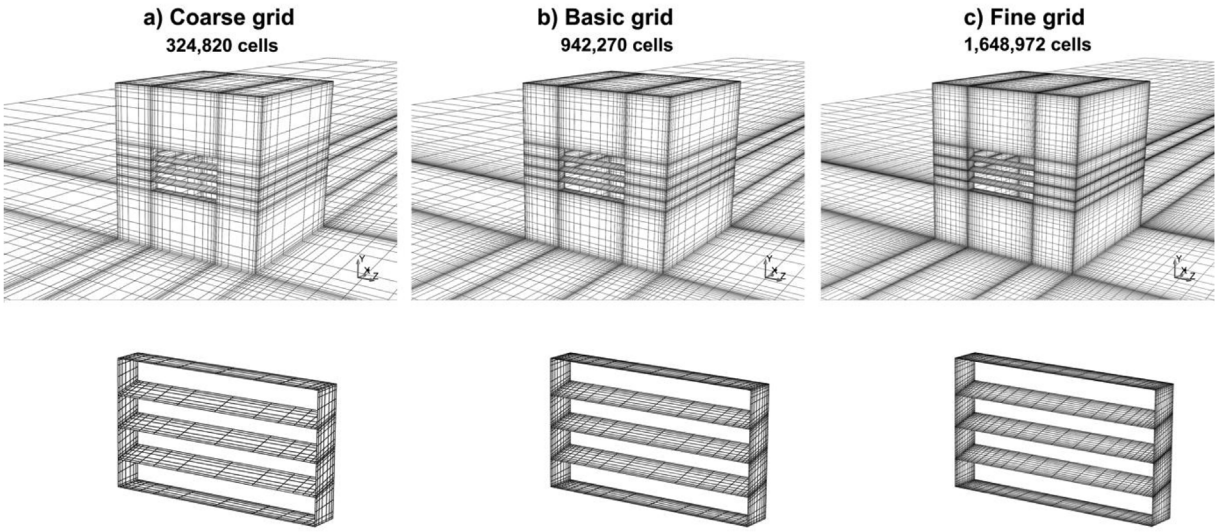


**Fig. 9.** Computational grids on building and louver surfaces and on bottom of domain as used for the grid-sensitivity analysis. (a) Coarse grid; 324,820 cells, (b) basic grid; 942,270 cells, (c) fine grid; 2,648,972 cells.

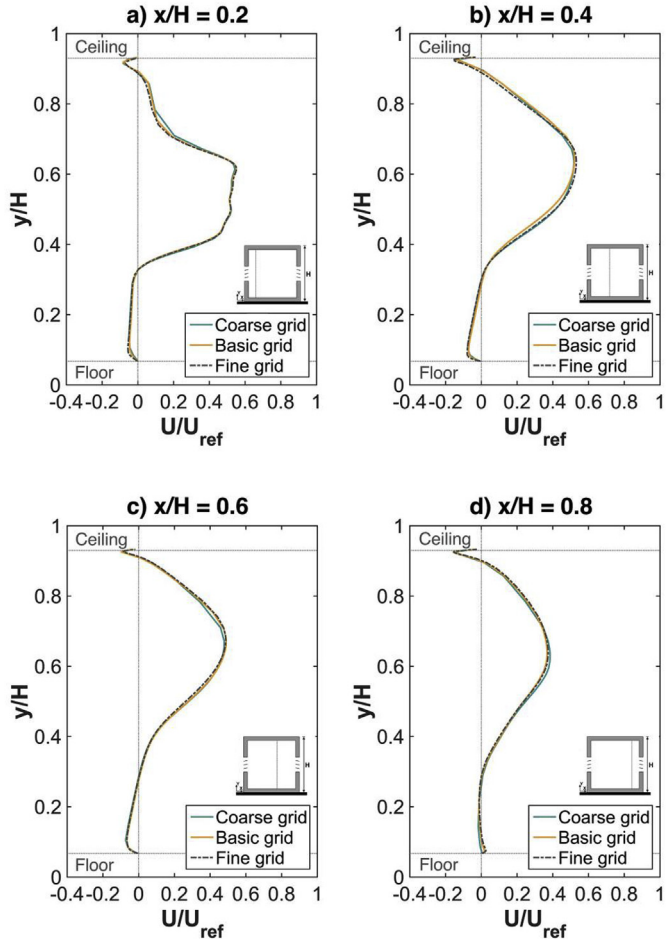


**Fig. 10.** Grid-sensitivity analysis for vertical profiles of the dimensionless streamwise mean velocity component, $U/U_{ref}$ along four lines in the vertical centerplane (z/H = 0.5) for the coarse grid (324,820 cells); basic grid (942,270 cells), fine grid (2,648,972 cells). (a) x/H = 0.2. (b) x/H = 0.4. (c) x/H = 0.6. (d) x/H = 0.8, $U_{ref}$ = 1.9 m/s.

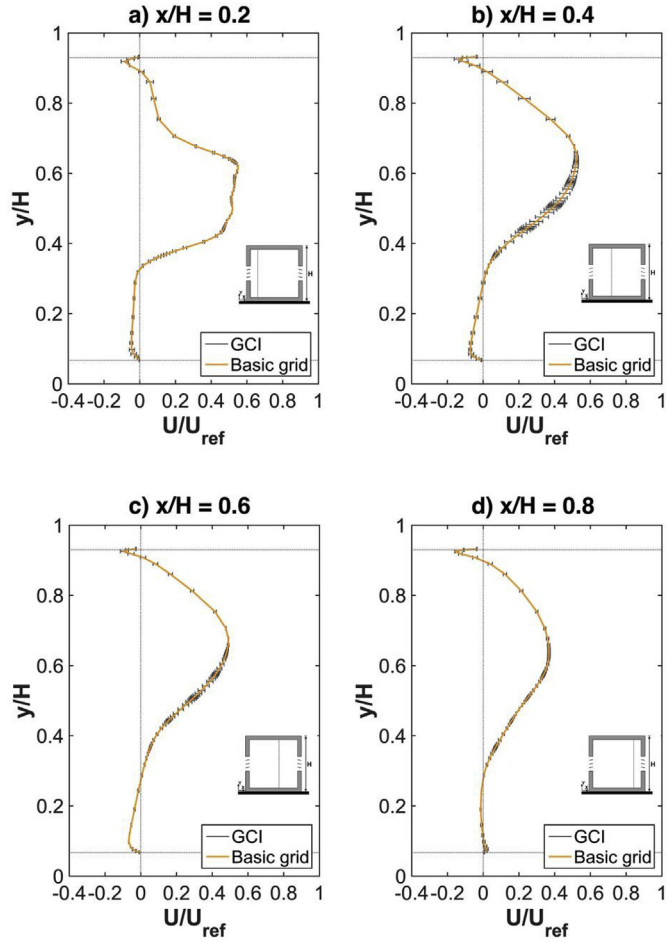


**Fig. 11.** Grid-convergence index (GCI) for vertical profiles of the dimensionless streamwise mean velocity component $U/U_{ref}$ along four lines in the vertical centerplane (z/H = 0.5) for the basic grid. (a) x/H = 0.2. (b) x/H = 0.4. (c) x/H = 0.6. (d) x/H = 0.8, $U_{ref}$ = 1.9 m/s.

then advected to the interior of the building and cause the irregular velocity profiles due to the louvers to be smeared out more rapidly than with the SST k-ω model. Fig. 12b–c shows the velocity profiles along the lines close to the center of the building ($0.4 \leq x/H \leq 0.6$). The width of the jet is reproduced by all three models; however, RSM predicts a slightly stronger downward deflection of the jet compared to RNG k-ε and SST k-ω, which is mainly visible along x/H = 0.6, where

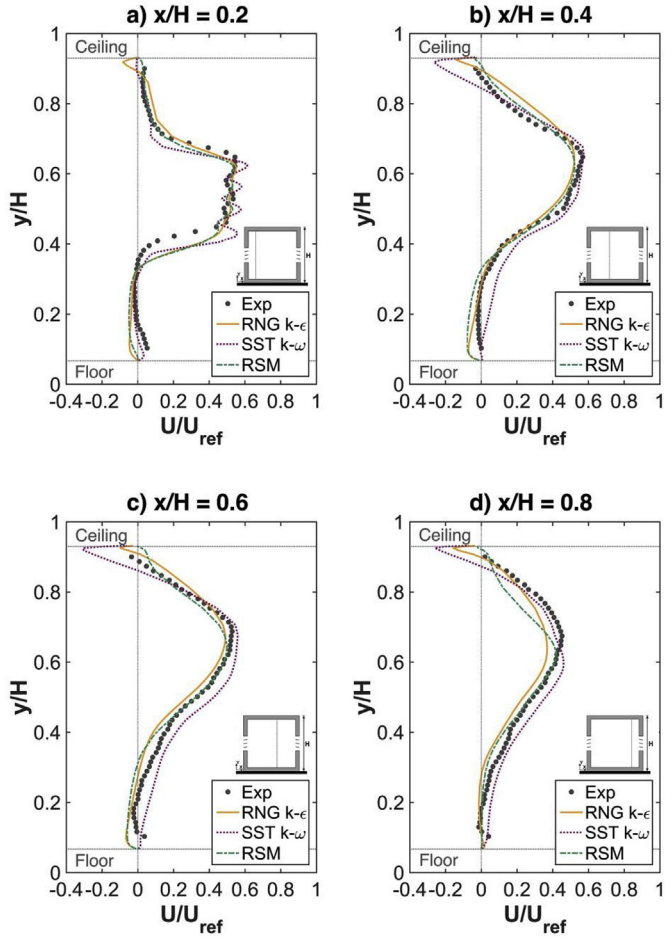


**Fig. 12.** Vertical profiles of dimensionless streamwise mean velocity component $U/U_{ref}$ along four lines in the vertical centerplane for configuration "Center": comparison of experiments vs. CFD with three different turbulence models. (a) x/H = 0.2. (b) x/H = 0.4. (c) x/H = 0.6. (d) x/H = 0.8, $U_{ref}$ = 1.9 m/s.

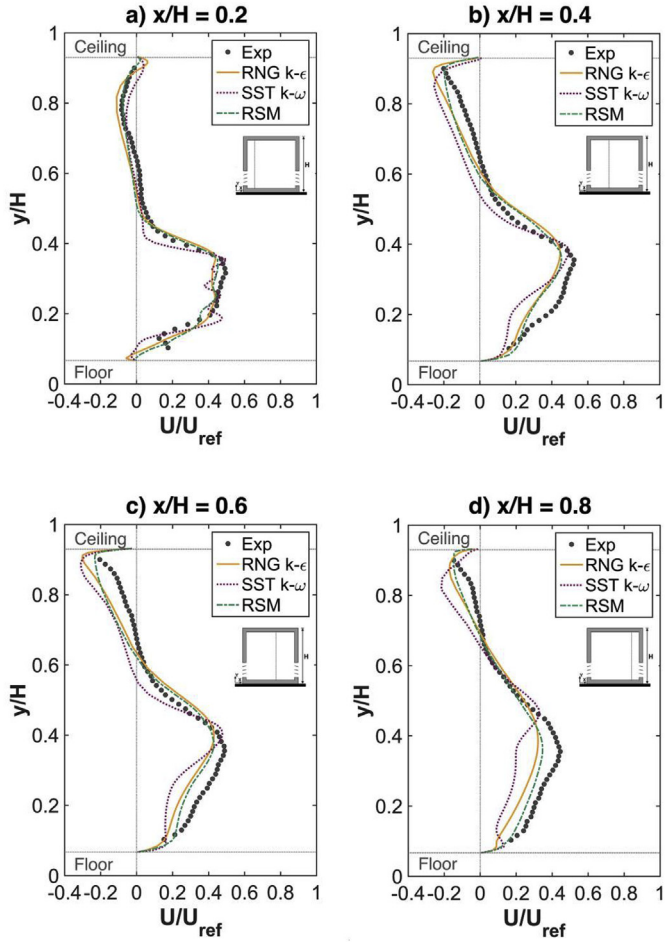


**Fig. 14.** Vertical profiles of dimensionless streamwise mean velocity component U/Uref along four lines in the vertical centerplane for configuration "Down": comparison of experiments vs. CFD with three different turbulence models. (a) x/H = 0.2. (b) x/H = 0.4. (c) x/H = 0.6. (d) x/H = 0.8, $U_{ref}$ = 1.9 m/s.

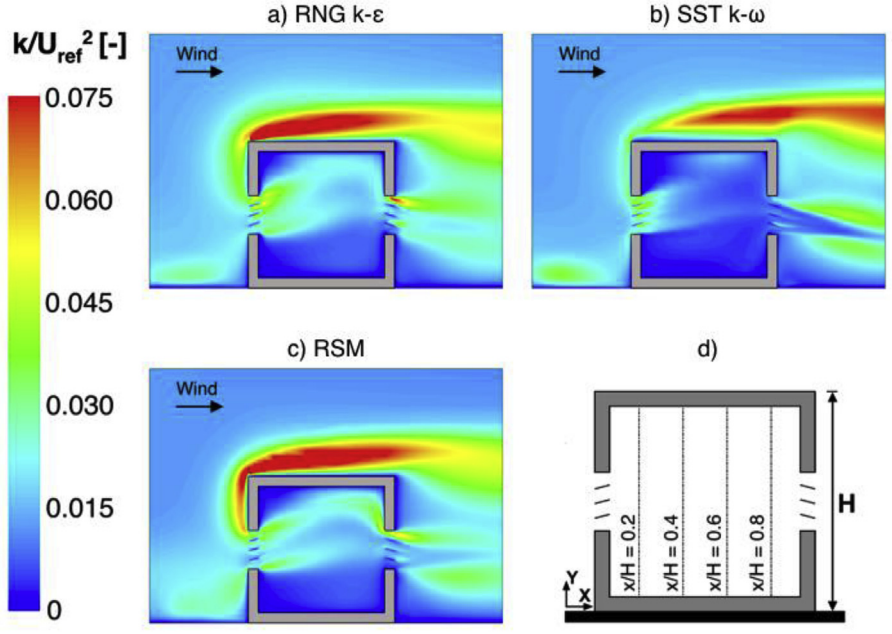


**Fig. 13.** Comparison of $k/U_{ref}^2$ in the vertical centerplane (z/H = 0.5) for configuration "Center" obtained with three different turbulence models, $U_{ref}$ = 1.9 m/s.

the location of maximum velocity is at y/H = 0.64 for RSM, while at y/H = 0.68 for RNG k-ε and SST k-ω. In addition, the SST k-ω and RSM models predict a lower location of the maximum velocity at x/H = 0.8 (y/H = 0.59 and y/H = 0.63 respectively) compared to the experimental data (y/H = 0.65). Overall, all turbulence models provide a fair to good prediction of the vertical profiles of streamwise velocity.

The results for configuration "Down" are depicted in Fig. 14. The effect of the individual louver slats is again visible along the vertical line at x/H = 0.2 for the SST k-ω model and it vanishes further downstream as in the building with the openings in the center of the facades. Overall, RNG k-ε and RSM show a better prediction of the shape and width of the jet compared to SST k-ω. All three models underpredict the maximum streamwise velocity in the jet region along the lines 0.4 ≤ x/H ≤ 0.8, however, it is most notable at x/H = 0.8 where $U/U_{ref}$ is underpredicted with up to 27.8% by RNG k-ε. In addition, some differences are present between the shape of the jet profiles obtained from PIV and those from SST k-ω at 0.4 ≤ x/H ≤ 0.8. Moreover, the maximum streamwise velocity predicted by SST k-ω is 26% lower at x/H = 0.8 and y/H = 0.53 compared to the experiments.

Fig. 15 shows the vertical profiles of the dimensionless streamwise mean velocity $U/U_{ref}$ for configuration "Up". Also for this configuration the influence of the individual louver slats is visible at x/H = 0.2 for the experimentally obtained velocities, however, for this configuration all three turbulence models predict this influence to a certain extent. This can be related to the much higher mean velocities in the jet in this configuration. The effect vanishes further downstream as observed for the other configurations. The maximum velocities and the shape of the jet are reasonably well predicted along x/H = 0.2 yielding 6.2% (SST k-ω) and 1.0% (RSM) difference in maximum velocity compared to the experimental results. Maximum velocities along the other three lines (x/H = 0.4, 0.6 and 0.8) are predicted well, however, the location of maximum velocity predicted by CFD is slightly lower for all cases except for SST k-ω along x/H = 0.4. SST k-ω and RNG k-ε overestimate the maximum velocities along all four lines up to 7.2% (RNG k-ε along x/H = 0.4). The RSM on the other hand underestimates the maximum velocities along all four lines up to 7.3% (along x/H = 0.6 and x/H = 0.8). Compared to the experiments, CFD predicts a wider wall jet in the upper part of the building (0.7 ≤ y/H ≤ 0.95) for all three turbulence models. In addition, the measurement resolution prohibits a detailed comparison with results obtained by CFD near the ceiling (boundary layer flow). In addition, some clear discrepancies between the experimental and numerical results are present in the shear layer close to the floor, which can most probably be attributed to a too low measurement resolution in this region.

The vertical profiles of the dimensionless streamwise mean velocity $U/U_{ref}$ for configuration "UpDown" are shown in Fig. 16. As for two of the previous configurations, the effect of the individual louver slats is visible along the line x/H = 0.2, but disappears further downstream. All three turbulence models overestimate the maximum velocity along the lines x/H = 0.2, 0.4 and 0.6, however, the maximum velocity along x/H = 0.8 is underpredicted by up to 26.3% (RSM). Overall, CFD predicts a lower location of the maximum velocity for all three models along all four lines, except for SST k-ω, where the location is almost identical (exp.: y/H = 0.87; SST k-ω: y/H = 0.88). The velocity profile along the vertical line changes at x/H = 0.8 as the air is exiting the building through the leeward opening (Fig. 16d). As mentioned above, the limited measurement resolution used (32 × 32 pixels) prohibits a detailed comparison of experimental and numerical results in the regions with large velocity gradients (boundary and shear layer).

### 5.2. Validation metrics

In order to obtain a quantitative evaluation of the performance of the three RANS turbulence models tested in this study, four validation metrics are used: the factor of 2 of observations (FAC2), the factor of 1.3 of observations (FAC1.3), the normalized mean square error (NMSE) and the fractional bias (FB) [50]. Note that NMSE and FB cannot be used for cases where the velocity reaches both positive and negative values [50]; therefore, it is used only for a specific part of the flow domain, as discussed later in this section. The metrics are calculated using the following equations (Eq. (9) – Eq. (12)).

$$FAC2 = \frac{1}{N}\sum_{i=1}^{N} n_i \quad with\ n_i = \begin{Bmatrix} 1\ for\ 0.5 \le \frac{P_i}{O_i} \le 2 \\ 0\ else \end{Bmatrix} \tag{9}$$

$$FAC1.3 = \frac{1}{N}\sum_{i=1}^{N} n_i \quad with\ n_i = \begin{Bmatrix} 1\ for\ 0.77 \le \frac{P_i}{O_i} \le 1.3 \\ 0\ else \end{Bmatrix} \tag{10}$$

$$NMSE = \frac{\overline{(O_i - P_i)^2}}{\overline{O_i}\,\overline{P_i}} \tag{11}$$

$$FB = \frac{\overline{O_i} - \overline{P_i}}{0.5(\overline{O_i} + \overline{P_i})} \tag{12}$$

with $O_i$ the observed (measured) value and $P_i$ the predicted value (CFD). The overbar denotes averaging over the whole dataset. The results are depicted in Table 1 for the velocities along four vertical lines (x/H = 0.2, 0.4, 0.6, 0.8) with indication of the ideal values. The best agreement with the experimental data according to FAC2 is achieved with RSM (0.80) and RNG k-ε (0.79) for configuration "Down". The RSM model shows the best agreement with the experimental data for configurations "Center", "Down" and "Up" while for configuration "UpDown" the agreement for RSM is only marginally lower compared

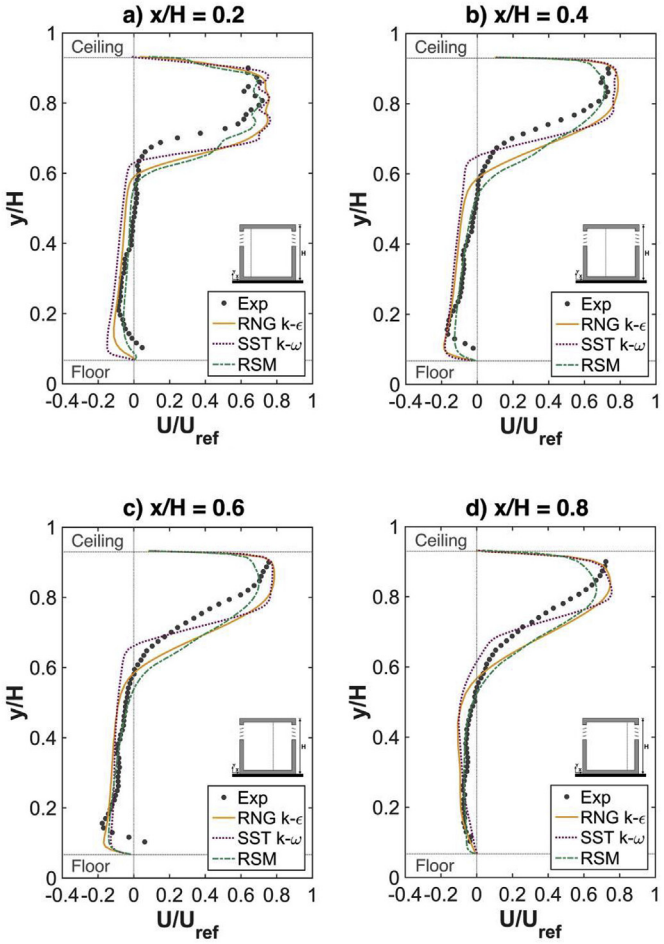


**Fig. 15.** Vertical profiles of dimensionless streamwise mean velocity component $U/U_{ref}$ along four lines in the vertical centerplane for configuration "Up": comparison of experiments vs. CFD with three different turbulence models. (a) x/H = 0.2. (b) x/H = 0.4. (c) x/H = 0.6. (d) x/H = 0.8, $U_{ref}$ = 1.9 m/s.

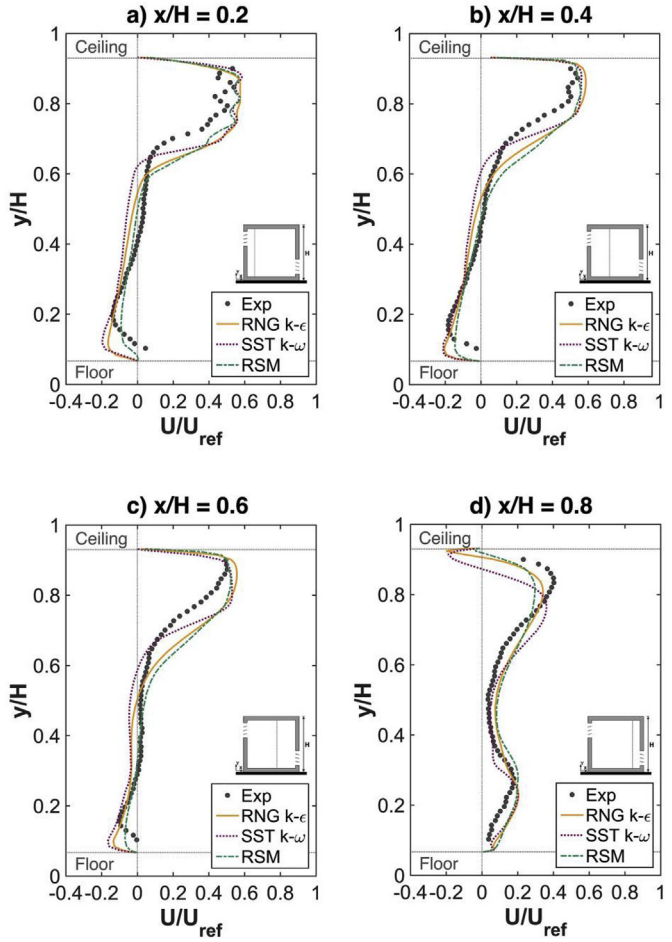


**Fig. 16.** Vertical profiles of dimensionless streamwise mean velocity component $U/U_{ref}$ along four lines in the vertical centerplane for configuration "UpDown": comparison of experiments vs. CFD with three different turbulence models. (a) x/H = 0.2. (b) x/H = 0.4. (c) x/H = 0.6. (d) x/H = 0.8, $U_{ref}$ = 1.9 m/s.

**Table 1**
Validation metrics for $U/U_{ref}$: factor of 2 of observations (FAC2).

| Ideal value | FAC2 | | | |
|---|---|---|---|---|
| | 1 | | | |
| | Center | Down | Up | UpDown |
| RNG k-ε | 0.72 | 0.79 | 0.70 | 0.75 |
| SST k-ω | 0.71 | 0.64 | 0.68 | 0.72 |
| RSM | 0.73 | 0.80 | 0.77 | 0.74 |

to RNG k-ε, which shows the best agreement for this configuration.

To get a better insight in the agreement of numerical results with the experimental data in the jet region, which is the region of main interest from a ventilative cooling perspective, a region of interest (ROI) is defined as the region where measured velocities are larger or equal to 50% of the maximum measured velocity ($U_{max}$) along a given vertical line.

Table 2 shows $FAC2_{ROI}$ and $FAC1.3_{ROI}$. $FAC2_{ROI}$ for all models and all configurations is within the range 0.80–1. RNG k-ε shows the highest values of $FAC2_{ROI}$ for configuration "Center". For configurations "Down" and "Up", the performance of RNG k-ε is identical to RSM and SST k-ω, respectively. However, for configuration "UpDown" the best agreement with experimental data is achieved by RSM.

The lowest value (0.80) is obtained by SST k-ω for configuration "Down". $FAC1.3_{ROI}$ shows similar results with the highest value for RNG k-ε (0.98) for configuration "Center" and the lowest value (0.46) for SST k-ω obtained for the configuration "Down". In this case, the RSM model shows the best performance for configurations "Down", "Up" and "UpDown".

$FB_{ROI}$ and $NMSE_{ROI}$ are shown in Table 3. For $FB_{ROI}$ the best performance is achieved by SST k-ω for configuration "Center" (−0.06), while RSM shows the best performance for configurations "Down" (0.14) and "Up" (−0.14), and RNG k-ε for "UpDown" (0.09). In case of $NMSE_{ROI}$ the same value is achieved by all three models for configuration "Center" while for the three other configurations the best agreement is obtained by RSM followed by RNG k-ε. The best agreement with experimental results (based on Tables 1–3) is achieved by RSM for configurations "Down", "Up" and "UpDown" and by RNG k-ε for configuration "Center". The performance of SST k-ω is slightly worse than RSM and RNG and thus the least satisfactory in this case.

The validation metrics quantify the agreement of the experimental data with the data obtained by the CFD simulations. In most cases, the best agreement is achieved by RSM. Table 1 shows that it outperformed the other two models for three configurations ("Center", "Down" and "Up"). While the results for $FAC2_{ROI}$ are very similar across all three models and the four configurations, for $FAC1.3_{ROI}$ RSM again outperforms the other two models for three configurations ("Down", "Up" and "UpDown"). According to $FB_{ROI}$ and $NMSE_{ROI}$ as presented in Table 3, RSM outperforms RNG k-ε and SST k-ω in two ("Down" and "Up") and three configurations ("Down", "Up" and "UpDown"), respectively. Based on these results, it can be concluded that overall RSM provides the best agreement with the experimental data.

### 5.3. Comparison: experiments vs. RSM

A comparison of the mean velocity vector field in the vertical centerplane as obtained by experiments and RSM is depicted in Fig. 17. The mean velocity vectors for configuration "Center" are shown in Fig. 17a–b, indicating that the main flow features are correctly reproduced by CFD. Fig. 17b clearly shows upward jet deflection, similarly as observed in the experiments. However, the jet deflection angle obtained with RSM is 16° while for the experiments the jet deflection angle is 19°. Fig. 17c–d shows the mean velocity vectors for configuration "Down". Again, the main flow features are well predicted by CFD. Experiments and CFD show that the jet is deflected slightly upwards after passing through the windward opening, the experimental results yield a jet deflection angle of 12°, while the numerical results obtained by RSM yield a jet deflection angle of 14°. In the experiments, only a small part of the jet is attached to the leeward wall and consequently a large recirculation zone above the jet is formed with a center at x/H ≈ 0.67 and y/H ≈ 0.68. Similarly, the recirculation zone is predicted by CFD, however, its core is in a slightly different position compared to the experiments (x/H ≈ 0.63 and y/H ≈ 0.64).

Configuration "Up" is shown in Fig. 17e–f. Both experiments and CFD simulations show that the flow is dominated by the jet attached to the ceiling and that the mean velocity increases when passing through the windward opening. A low velocity zone is observed below the jet – both in experiments and CFD – suggesting that there is almost no

**Table 2**
Validation metrics for $U/U_{ref}$: FAC2 and FAC1.3 in the region of interest.

| Ideal value | $FAC2_{ROI}$ | | | | $FAC1.3_{ROI}$ | | | |
|---|---|---|---|---|---|---|---|---|
| | 1 | | | | 1 | | | |
| | Center | Down | Up | UpDown | Center | Down | Up | UpDown |
| RNG k-ε | 1.00 | 1.00 | 1.00 | 0.98 | 0.98 | 0.56 | 0.75 | 0.69 |
| SST k-ω | 0.98 | 0.80 | 1.00 | 0.92 | 0.93 | 0.46 | 0.75 | 0.67 |
| RSM | 0.98 | 1.00 | 1.00 | 1.00 | 0.85 | 0.93 | 0.85 | 0.71 |

**Table 3**
Validation metrics for $U/U_{ref}$: fractional bias (FB) and normalized mean square error (NMSE) in the region of interest (ROI).

| Ideal value | $FB_{ROI}$ | | | | $NMSE_{ROI}$ | | | |
|---|---|---|---|---|---|---|---|---|
| | 0 | | | | 0 | | | |
| | Center | Down | Up | UpDown | Center | Down | Up | UpDown |
| RNG k-ε | 0.07 | 0.17 | −0.24 | 0.09 | 0.02 | 0.05 | 0.04 | 0.06 |
| SST k-ω | −0.06 | 0.28 | −0.24 | 0.15 | 0.02 | 0.15 | 0.04 | 0.11 |
| RSM | 0.08 | 0.14 | −0.14 | 0.14 | 0.02 | 0.03 | 0.02 | 0.05 |

mixing in the largest part of the room. The jet deflection angle obtained with RSM is 10°, while for the experiments the jet deflection angle is 17°. Finally, configuration "UpDown" is shown in Fig. 17g–h. In both experiments and CFD, the jet attaches to the ceiling under a jet deflection angle of 10° immediately after passing through the windward opening. CFD predicts a stronger and less deflected jet (four degrees smaller angle) than the one observed in the experiments. However, both experiments and CFD show that a large recirculation zone contributing to the mixing flow is formed below the jet.

### 5.4. Velocity contour plots

Fig. 18 shows contours of dimensionless mean velocity magnitude $|V|/U_{ref}$ in the vertical centerplane for each window position as obtained with RSM, which is found to be the best overall turbulence model for the cross-ventilation cases studied in this paper based on the validation metrics. In all four configurations, the jet is deflected upwards due to the angle of the louver slats.

Fig. 18a shows configuration "Center", in which the flow is directed upwards immediately after passing through the windward opening and a region with low velocities is formed under the jet. A similar trend can be observed for configuration "Down" (Fig. 18b). The jet is directed upwards, however, close to the leeward opening, the majority of the flow is directed towards the leeward opening, while a small secondary jet attaches to the leeward and ceiling wall forming a large recirculation zone above the primary jet.

Configuration "Up" is shown in Fig. 18c. In this configuration, the jet is attached to the ceiling and passes directly from windward to leeward opening. The velocity of the jet is clearly higher compared to the two previous configurations (Fig. 18a–b), which can be attributed to the reasons mentioned earlier, i.e. less jet spreading and a larger pressure difference between the windward and the leeward opening. In addition, the internal flow resistance in this configuration is substantially lower than in configuration "UpDown", resulting in higher velocities (+56% close to the leeward opening) in the "Up" configuration compared to the "UpDown" configuration. A region with very low velocities is formed below the jet in the "Up" configuration (($|V|/U_{ref} < 0.13$).

Fig. 18d shows configuration "UpDown". The jet is attached to the ceiling and leeward wall with locally high velocities around and downstream of the louvers in the leeward opening.

## 6. Dimensionless airflow rate and air exchange efficiency

The age of air is calculated to assess the air exchange efficiency for each configuration based on the CFD simulations using the RSM turbulence model. The age of air is a statistical concept measuring the air quality in a given point [51] and for this case, it is determined by solving an Eulerian advection-diffusion equation for a passive scalar in ANSYS Fluent. The turbulent Schmidt number ($Sc_t$) is equal to 0.7 and is assumed to be constant in the entire domain [52,53].

In order to provide a more extensive description of the influence of the louvers on the age of air, additional CFD simulations are conducted for the same four opening configurations but without louvers in the window openings. The computational setup is identical to the one described in Section 4, however, simulations are performed using only RSM as it showed the overall best agreement with the experimental data for the configuration with louvers.

Fig. 19a–b shows the age of air (τ) in the vertical centerplane for configurations "Center" with and without louvers, respectively. Fig. 19a shows a small zone at the bottom part close to the windward opening where the age of air exceeds 2 s, while the air is relatively fresh ($\tau < 0.7$ s) in the upper part close to the leeward opening due to deflection of the jet caused by the louvers. A very small zone with an age of air exceeding 2 s in the upper corner close to the windward opening is visible in Fig. 19b for configuration "Center" without louvers. Contrary to the simulation with louvers, the jet is directed downwards bringing the fresh air to the lower part of the building. As a result, the area above the jet shows locations with age of air values around 1–2 s.

In configuration "Down" (Fig. 19c–d), the fresh air is mainly located in the lower part of the building near the windward opening. In this configuration, the louvers have the largest influence on the age of air. They direct the flow upwards, forcing the fresh air to be more extensively mixed with the air in the building resulting in fresher air ($1\text{ s} < \tau < 2\text{ s}$) above the jet. On the contrary, in the case without louvers (Fig. 19d), the flow is short-circuiting between the windward and leeward opening without significant mixing within the room, which results in an age of air of more than 2 s above the jet.

Configuration "Up" (Fig. 19e–f) does not induce sufficient mixing of air but rather a short-circuiting flow for both cases, with and without louvers, i.e. the air exits the room without strong mixing (as can be seen in Fig. 18c), which is confirmed by the values of the age of air. The air exiting through the leeward opening is relatively fresh ($0.35\text{ s} < \tau < 1.3\text{ s}$), while the air under the jet is not (1.5 s to more than 2 s, where the area with an age of air higher than 2 s is only present close to the windward wall for the case with louvers). Moreover, configuration "Up" without louvers shows a larger area under the jet where the age of air exceeds 2 s, indicating that there is almost no mixing of air inside the building.

Fig. 19g–h shows the age of air for configuration "UpDown". Relatively low values of age of air ($\tau < 1.5$ s) for configuration "UpDown" for both cases, with and without louvers, are present compared to the other configurations. This can be attributed to the position of the windows where the fresh air enters the building in the upper part of the windward facade and is forced to flow downwards to exit the building. Because of this, a high-momentum jet is formed which then drives a recirculation zone inside the building resulting in relatively well-mixed air within the space. In this case, the louvers have only a fairly limited influence on the age of air inside the building.

Fig. 20 shows the dimensionless volume flow rate and the air exchange efficiency for all four configurations with and without louvers as computed with CFD with RSM. The dimensionless volume flow rate is calculated using Eq. (12) [16]:

$$DFR = Q/(U_{ref} \cdot A_w) \quad (13)$$

where Q [$m^3/s$] is the volume flow rate through the building obtained by CFD with RSM, $U_{ref}$ is the reference velocity equal to 1.9 m/s and $A_w$ [$m^2$] is the area of the opening (0.0028 $m^2$). Fig. 20 shows that the configurations without louvers, except for configuration "Up", provide higher dimensionless volume flow rates. This is due to the larger "free area" of the opening compared to the opening with louvers but also to the changed direction of the jet and the resulting flow resistances through the windward and leeward opening and inside the building volume.

The highest dimensionless volume flow rate (0.69– reduced-scale value for case with louvers and 0.68 for case without louvers) is present for the building with openings in the upper part of the facade. This can be attributed to the higher pressure difference between the windward and leeward opening, as the windward opening is located close to the

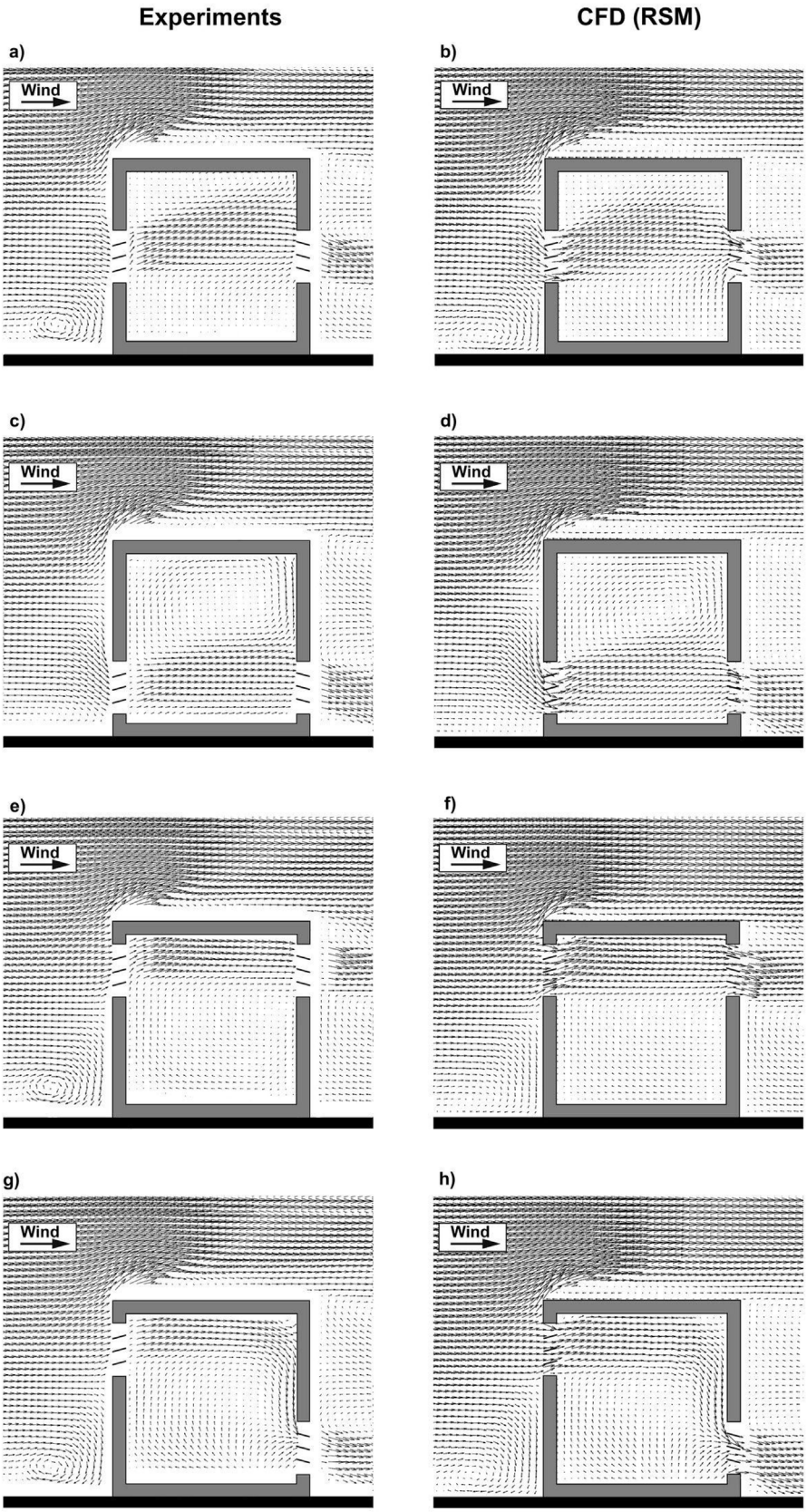


**Fig. 17.** Comparison of mean velocity ($|V|/U_{ref}$) vector fields in vertical centerplane for all four configurations obtained by experiments (a, c, e, g) and CFD (RSM) (b, d, f, h).

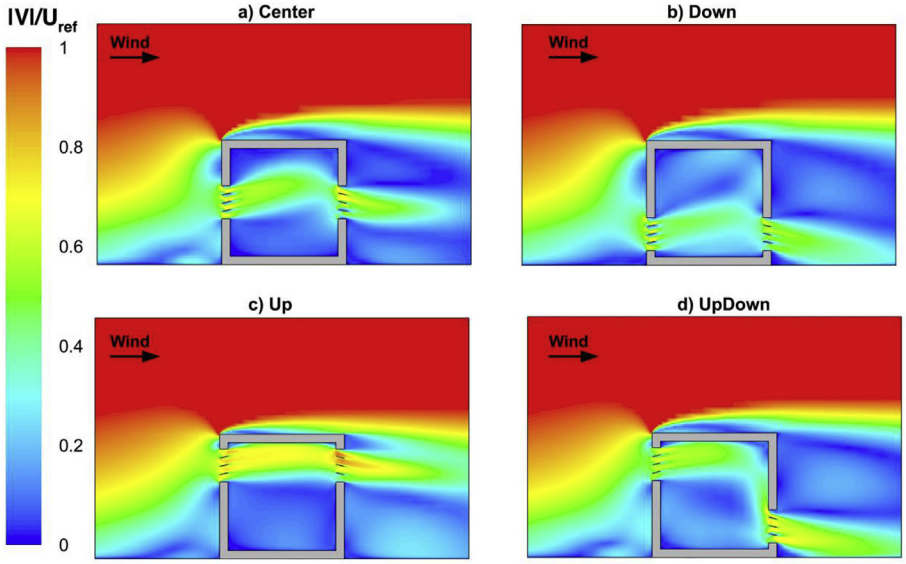


**Fig. 18.** Contours of dimensionless mean velocity magnitude ($|V|/U_{ref}$) in the vertical centerplane for four configurations: (a) "Center", (b) "Down", (c) "Up" and (d) "UpDown". Contour plots are obtained using the RSM turbulence model, $U_{ref}$ = 1.9 m/s.

stagnation area, and to the lower flow resistance. The dimensionless volume flow rate obtained for configuration "Down" (0.38) is 46% lower compared to the building with openings in the upper part for the case with louvers. This can be attributed to the fact that there are low velocity areas outside of the building near the position of the windward opening. In the case without louvers, the dimensionless volume flow rate for configuration "Down" is 0.47, which is 23.7% more than in the same configuration but with louvers. Again, this difference in the dimensionless volume flow rate can be attributed to the presence of louvers, which reduces the "free area" of the opening and to the changed direction of the jet and the resulting flow resistances through the windward and leeward opening and inside the building volume.

The dimensionless volume flow rate obtained in a building with the openings in the center of the facade is 0.47 for the case with louvers, while the dimensionless volume flow rate for the configuration "Center" without louvers is 0.49 (4.3% higher).

Configuration "UpDown" provides a dimensionless volume flow rate of 0.47 for the case with louvers and 0.50 for the case without louvers, yielding a 6.4% difference.

The air exchange efficiency for all four configurations (with and without louvers) is calculated using Eq. (13) [54]:

$$\varepsilon_A = 100 \cdot \frac{\tau_{out}}{2\tau_{av}}[\%] \tag{14}$$

where $\tau_{out}$ is the age of air at the leeward opening and $\tau_{av}$ is the volume averaged age of the air in the building.

The highest air exchange efficiency (45%) is obtained by configuration "Center" for the case with louvers and by configuration "UpDown" for the case without louvers (45%). In both cases, the air in the room is relatively well mixed as a result of the location of the openings, allowing the incoming fresh air to mix within the indoor air rather than being flushed out almost directly. The air exchange efficiency for configuration "Center" with louvers is 2.8% higher, i.e. 45% compared to 42.2% for the same case without louvers. This can be attributed to the louvers, which direct the flow to the upper part of the building inducing stronger mixing than in the case without louvers. The air exchange efficiency for configuration "UpDown" for the case without louvers is only slightly higher than for the case with louvers (45% vs. 44%).

The lowest air exchange efficiency is obtained for configuration "Up" (23% for case with louvers and 20% without louvers), which is caused by the short-circuiting flow; the air is not sufficiently mixed and fresh air leaves the room almost immediately, while unventilated areas are present below the jet.

The highest absolute difference (9.1%) between the case with and without louvers is for the configuration "Down". In the case with louvers, the incoming fresh air is directed upwards where it is mixed with the air inside of the building, while in the case without louvers the flow is short-circuiting through the building without any significant mixing.

## 7. Discussion

The objective of this study is threefold: (1) to present wind-tunnel experiments of cross-ventilation of a generic isolated cubic building equipped with louvers for three symmetric and one asymmetric window opening configuration, (2) to validate CFD simulations for all configurations with the wind-tunnel experiments and (3) to investigate the impact of window opening positions and louvers on indoor airflow pattern, age of air, dimensionless volume flow rate and air exchange efficiency.

To the best knowledge of the authors, this is the first study to investigate the influence of opening position on the cross-ventilation and indoor airflow in a building equipped with ventilation louvers. This study has provided interesting insights into cross-ventilation in generic buildings equipped with louvers.

The performance of three turbulence models (RNG k-ε, SST k-ω and RSM) was tested. Overall, all three turbulence models provide good agreement with the experimental data, however, the best performance is achieved by RSM. These findings are in line with results by Lee at al. [29], however, they are in contradiction with the previous findings by Meroney [16], van Hooff et al. [19] and Ramponi and Blocken [20]. Note that these studies were performed for fully opened windows without shading devices such as louvers, which, as shown in the present study, can have an impact on the indoor airflow. Moreover, comparison with different studies is often complicated due to the different geometry of the building, different opening configurations, the presence of shading devices (such as louvers for example) and/or the wide range of computational parameters, which can influence the outcome of the simulation.

The highest dimensionless volume flow rate is achieved by configuration "Up" for both cases, i.e. with and without louvers. This is in line with findings by Meroney [16] considering results from RANS simulations. However, Meroney [16] reported the lowest dimensionless volume flow rate for configuration "UpDown", while in the present study, this configuration has second highest dimensionless volume flow rate for the case with and without louvers. In addition, this study shows that although configuration "Up" has highest dimensionless volume flow

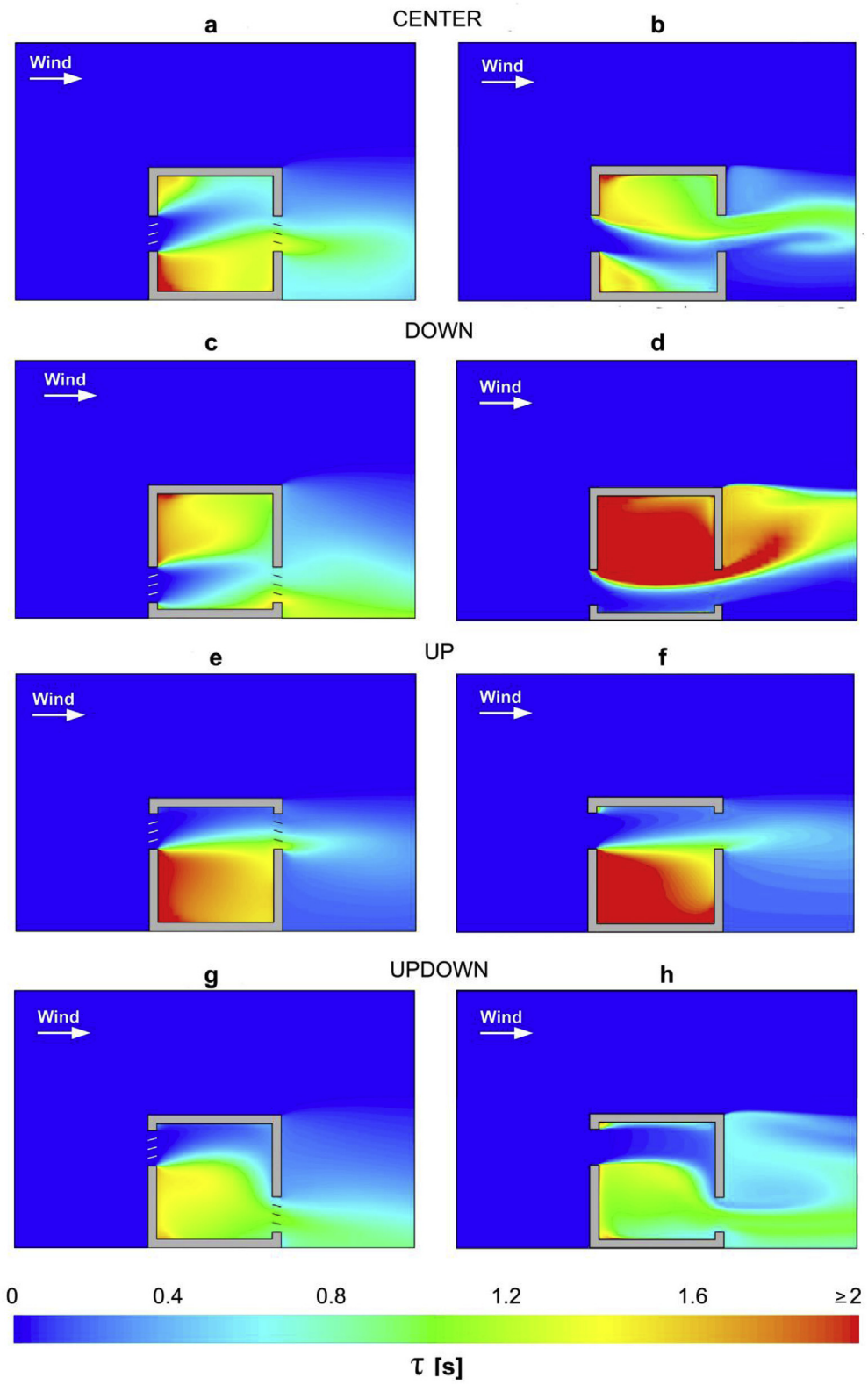


**Fig. 19.** Contours of age of air in the vertical centerplane for the four configurations: (a,b) "Center", (c,d) "Down", (e,f) "Up" and (g,h) "UpDown", for the case with louvers (a,c,e,g) and the case without louvers (b,d,f,h).

rate, it has the lowest air exchange efficiency due to the short-circuiting of air and insufficient mixing of air inside the building.

However, it is necessary to mention some limitations of this study, which should be addressed in future work.

- The wind-tunnel experiments and simulations were carried out under isothermal conditions. In future research, the impact of opening positions on heat removal effectiveness will be addressed. In addition, the balance between wind-driven and buoyancy-driven natural ventilation flow will be assessed for a range of

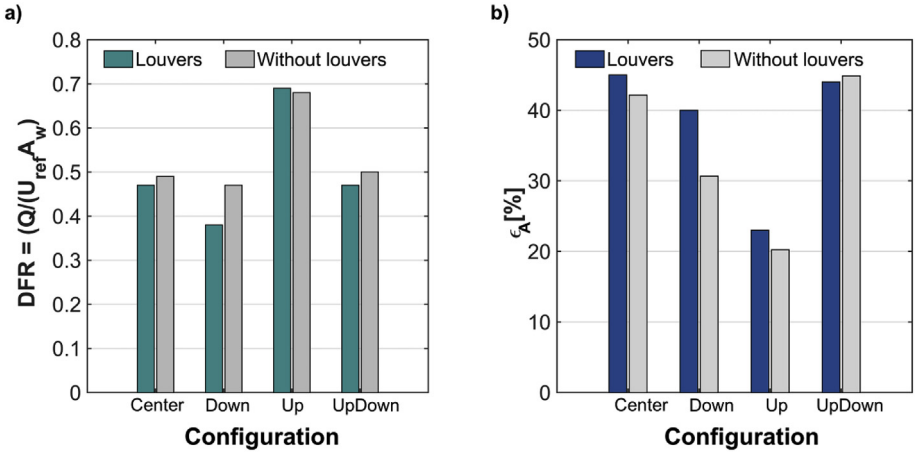


**Fig. 20.** (a) Dimensionless volume flow rate (DFR) and (b) air exchange efficiency ($\varepsilon_a$) for all four configurations obtained from steady RANS CFD in combination with RSM turbulence model. Results for the case with louvers and the case without louvers are included.

meteorological conditions (i.e. wind speed ($U_{ref}$), wind direction, ambient air temperature).

- The measurements were performed to obtain information about the flow pattern and velocities in the entire vertical centerplane. As a consequence, the measurement resolution (32 × 32 pixels) was not sufficient to fully capture the large velocity gradients in the shear layer of the incoming jet. Therefore, a detailed comparison between numerical and experimental results was not possible for the shear layer regions. Future work will include measurements in different regions of interest to capture these large spatial gradients.
- The measurements were performed only in the vertical centerplane. Future work will include measurements in the horizontal and some of the lateral vertical planes to investigate a possible effect of asymmetric or unstable flow.
- The study was performed for one specific building geometry and one specific louver geometry. Atmospheric boundary layer wind tunnel tests on buildings are unavoidably performed at reduced scale. In terms of dynamic similarity, it is widely accepted in ABL wind tunnel testing that Reynolds numbers do not need to match exactly. Moreover, exact matching is often impossible given physical constraints and the upper speed limit of the wind tunnel facility. It is generally accepted that if the building model has sharp edges and if the building Reynolds number at reduced scale is above 11,000, the flow field can be considered Reynolds number independent [55,56]. Concerning the scaling of louvers, the situation is more complicated. In reality, louvers will operate under a wide range of local Reynolds numbers, which can be based on louver depth. Small louvers with a depth of 0.1 m and exposed to a low speed U = 0.1 m/s at 15 °C yield a local Reynolds number of 690, while larger louvers with a depth of 0.2 m and exposed to U = 3 m/s yield a local Re of 41,380. It is therefore clear that louvers can be exposed at a wide range of Reynolds numbers, in the laminar, transitional or turbulent regime, and above or below the 11,000 Re number threshold. In the present study, the model louver geometry was chosen based on two criteria: (1) obtain a louver Reynolds number in the range of realistic values and (2) manufacturability. The resulting model louver Reynolds number in the present study was about 1,310. It is clear that this single louver Re number cannot represent the entire range of possible Reynolds numbers. However, it should be noted that the main effect of the louvers in the present study is changing the direction of the incoming ventilation jet, and this effect is already evident at Re = 1,310. At larger Reynolds numbers (larger speed or larger louver depth), this effect will not be less pronounced, which suggests that the results presented in this paper have a wider (Re number) range of applicability. Nevertheless, future work will focus on different louver slat angles and slat sizes, with a specific emphasis on the effect of the ratio between window/building size and slat size on the indoor airflow pattern.
- Future work will focus on different louver slat angles and slat sizes, with a specific emphasis on the effect of the ratio between window/building size and slat size on the indoor airflow pattern. Although the louvers in the present study might appear large, it should be noted the commercially available louvers exist in a wide range of shapes and sizes and can even be larger compared to the window size as in the present study (Fig. 21).
- Additional turbulence models, such as the standard k-ε and realizable k-ε models will be included in future studies.
- The building under study is a generic isolated building rather than a real and specific building geometry. Although studies on generic isolated buildings are standard practice in CFD studies in wind engineering and building simulation [35–37,40–42] as well as in building energy simulation studies (e.g. BESTEST [57]), future work can consider real and specific building geometries. In terms of

**Fig. 21.** Examples of large louvers (© Louvretec, reproduced with permission).

generic building geometries, these geometries are best taken identical or similar to those in previous studies to allow results intercomparison.

## 8. Conclusions

This study presents wind-tunnel experiments and CFD simulations of cross-ventilation in a generic isolated cubic building equipped with ventilation louvers. The experiments and simulations were carried out for four different opening positions:

- Building with openings in the center of the facade – configuration "Center".
- Building with openings in the bottom part of the facade – configuration "Down".
- Building with openings in the upper part of the facade – configuration "Up".
- Building with one opening in the windward facade and one opening in the leeward facade – configuration "UpDown".

Streamwise and vertical mean velocities in the vertical centerplane were measured in a wind tunnel using PIV. The 3D steady RANS simulations were carried out in a combination with three different turbulence models: RNG k-ε, SST k-ω and RSM. Dimensionless streamwise mean velocity profiles ($U/U_{ref}$) along four vertical lines were compared with the experimental results. In addition, the age of air, the dimensionless volume flow rate and the air exchange efficiency were calculated for each configuration based on the CFD simulations performed using the RSM turbulence model.

The following main conclusions can be drawn from this study:

- The flow in the building is dominated by the jet passing through the openings.
- The highest mean velocities are observed for configuration "Up" which can be attributed to (i) the position of the windward opening near the stagnation zone at the facade, inducing a higher pressure difference between the openings and thus resulting in higher velocities, (ii) the presence of the ceiling, inhibiting strong jet spreading and (iii) to the lower flow resistance in this configuration.
- The lowest mean velocities are measured for the configuration "Down", which can be attributed to the location of the windows in the low velocity region close to the ground.
- Overall, a very good agreement with the experimental data for all four configurations is shown in the region of interest (ROI; $U/U_{max} > 0.5$) and a fair to good agreement along the entire four vertical lines.
- Overall, CFD predicts lower deflection angles of the jet compared to the experiments in all configurations except for the configuration "Down", where the jet has a 2° higher deflection angle compared to the experiments.
- The validation metrics show that for most of the cases RSM outperforms RNG k-ε and SST k-ω. For FAC2, $FAC1.3_{ROI}$ and NMSE, RSM shows a better agreement with experimental data for three configurations while for FB it outperforms the other two models for two configurations. The results obtained for $FAC2_{ROI}$ show very similar results across all configurations and turbulence models.
- The least satisfactory agreement is obtained by the SST k-ω model. However, the SST k-ω model still predicts the mean velocities with reasonable accuracy and the agreement with experimental data is good. Hence, if necessary this model can be used for the simulation of cross-ventilation in buildings equipped with louvers.
- The largest dimensionless volume flow rate (0.69) is achieved for configuration "Up" for the case with louvers. The lowest volume flow rate (0.38) is obtained for configuration "Down" for the case with louvers.
- The largest influence of louvers on the dimensionless volume flow rate is observed for configuration "Down", where the dimensionless volume flow rate for the case with louvers is 23.7% lower compared to the case without louvers.
- A negligible influence of louvers is shown for configuration "Up", where the dimensionless volume flow rate for the case with louvers is only 1.4% higher compared to the case without louvers.
- The highest air exchange efficiency (45%) is obtained for configuration "Center" for the case with louvers and for configuration "UpDown" without louvers, closely followed by configuration "UpDown" with louvers (44%). This can be attributed to the good mixing within the room resulting from the positions of the windward and leeward window openings.
- The lowest air exchange efficiency is achieved for configuration "Up" (20%) for the case without louvers, which is due to the short-circuiting flow, resulting in almost no mixing within a large part of the building.
- The largest influence of louvers on the air exchange efficiency is present for configuration "Down", where the air exchange efficiency for the case with louvers is 9.1% higher compared to the case without louvers (39.8% vs. 30.7%). This is attributed to the louvers directing the incoming fresh air upwards and inducing mixing of air within the room.
- A very small influence of louvers on the air exchange efficiency is shown for configuration "UpDown", where the air exchange efficiency for the case with louvers is only slightly higher compared to the case without louvers (45% vs. 44%).
- Configuration "UpDown" has the lowest values of the age-of-air compared to the other three configurations, which is attributed to the position of openings resulting in well-mixed air in the room and therefore lack of stagnation areas.
- Configurations "Up" and "Down', both without louvers, on the other hand have low values of age-or-air only in the upper and lower part of the building respectively, where the position of the openings is inducing the short-circuiting flow. This results in a large area under the jet near the windward opening for the configuration "Up" with an age of air higher than 2 s. For the configuration "Down" without louvers, an area with an age of air higher than 2 s is present above the jet.

## Acknowledgement

Twan van Hooff is currently a postdoctoral fellow of the Research Foundation - Flanders (FWO) and acknowledges its financial support (project FWO 12R9718N). In addition, the authors gratefully acknowledge the partnership with ANSYS CFD. The authors are thankful to Geert-Jan Maas (Laboratory of the Unit Building Physics and Services) for the construction and development of the experimental building model and to Neil Gillam from University of Southampton for his help and support during the wind-tunnel experiments.

## References

[1] V. Costanzo, M. Donn, Thermal and visual comfort assessment of natural ventilated office buildings in Europe and North America, Energy Build. 140 (2017) 210–223.
[2] Z. Cheng, L. Li, W.P. Bahnfleth, "Natural ventilation potential for gymnasia – case study of ventilation and comfort in a multisport facility in northeastern United States, Build. Environ. 108 (2016) 85–98.
[3] G.R. Hunt, N.B. Kaye, Pollutant flushing with natural displacement ventilation, Build. Environ. 41 (9) (2006) 1190–1197.
[4] T. van Hooff, B. Blocken, CFD evaluation of natural ventilation of indoor environments by the concentration decay method: CO2 gas dispersion from a semi-enclosed stadium, Build. Environ. 61 (2013) 1–17.
[5] G. Chiesa, M. Grosso, Geo-climatic applicability of natural ventilative cooling in the Mediterranean area, Energy Build. 107 (2015) 376–391.
[6] A. Belleri, M. Avantaggiato, R. Lollini, "Ventilative cooling in shopping centers' retrofit: the Mercado Del val case study, Energy Procedia 111 (2017) 669–677.
[7] G. Carrilho da Graça, P. Linden, Ten questions about natural ventilation of non-domestic buildings, Build. Environ. 107 (2016) 263–273.
[8] A. Argiriou, Single-sided ventilation of buildings through shaded large openings, Energy 27 (2) (2002) 93–115.

[9] P.D. O'Sullivan, M. Kolokotroni, A field study of wind dominant single sided ventilation through a narrow slotted architectural louvre system, Energy Build. 138 (2017) 733–747.
[10] D. Chandrashekaran, Air Flow through Louvered Openings: Effect of Louver Slats on Air Movement inside a Space, Master Thesis University of Southern California, 2010.
[11] A. Tablada, J. Carmeliet, M. Baelmans, D. Saelens, Exterior Louvers as a Passive Cooling Strategy in a Residential Building : Computational Fluid Dynamics and Building Energy Simulation Modelling, Energy (2009) 22–24.
[12] P. Karava, T. Stathopoulos, A.K. Athienitis, Airflow assessment in cross-ventilated buildings with operable façade elements, Build. Environ. 46 (1) (2011) 266–279.
[13] Y. Tominaga, B. Blocken, Wind tunnel analysis of flow and dispersion in cross-ventilated isolated buildings: impact of opening positions, J. Wind Eng. Ind. Aerod. 155 (2016) 74–88.
[14] R. Ramponi, B. Blocken, CFD simulation of cross-ventilation flow for different isolated building configurations: validation with wind tunnel measurements and analysis of physical and numerical diffusion effects, J. Wind Eng. Ind. Aerod. 104–106 (2012) 408–418.
[15] M.Z.I. Bangalee, J.J. Miau, S.Y. Lin, M. Ferdows, Effects of lateral window position and wind direction on wind-driven natural cross ventilation of a building: a computational approach, J. Comput. Eng. 2014 (2014) 1–15.
[16] R.N. Meroney, CFD prediction of airflow in buildings for natural ventilation, 11th Americas Conference on Wind Engineering, 2009, pp. 1–11.
[17] N.F.M. Kasim, S.A. Zaki, M.S.M. Ali, N. Ikegaya, A.A. Razak, Computational study on the influence of different opening position on wind-induced natural ventilation in urban building of cubical array, Procedia Eng. 169 (2016) 256–263.
[18] J.I. Perén, T. van Hooff, B.C.C. Leite, B. Blocken, CFD analysis of cross-ventilation of a generic isolated building with asymmetric opening positions: impact of roof angle and opening location, Build. Environ. 85 (2015) 263–276.
[19] T. van Hooff, B. Blocken, Y. Tominaga, On the accuracy of CFD simulations of cross-ventilation flows for a generic isolated building: comparison of RANS, LES and experiments, Build. Environ. 114 (2016) 148–165.
[20] R. Ramponi, B. Blocken, CFD simulation of cross-ventilation for a generic isolated building: impact of computational parameters, Build. Environ. 53 (2012) 34–48.
[21] Y. Jiang, D. Alexander, H. Jenkins, R. Arthur, Q. Chen, Natural ventilation in buildings: measurement in a wind tunnel and numerical simulation with large-eddy simulation, J. Wind Eng. Ind. Aerod. 91 (3) (2003) 331–353.
[22] H. Cheng-hu, T. Kurabuchi, M. Ohba, Numerical study of cross-ventilation using two- equation RANS numerical study of cross-ventilation using two-equation RANS, Int. J. Vent. 4 (2) (2005) 123–132.
[23] G. Carrilho da Graca, Q. Chen, L.R. Glicksman, L.K. Norford, Simulation of wind-driven ventilative cooling systems for an apartment building in Beijing and Shanghai, Energy Build. 34 (1) (2002) 1–11.
[24] C.-H. Hu, M. Ohba, R. Yoshie, CFD modelling of unsteady cross ventilation flows using LES, J. Wind Eng. Ind. Aerod. 96 (10–11) (2008) 1692–1706.
[25] I.T. Kurabuchi, M. Ohba, A. Arashiguchi, Numerical study of airflow structure of a cross ventilated model building, Proceedings of Air Distribution in Rooms: Ventilation for Health and Sustainable Environment, 2000, pp. 313–318.
[26] G. Evola, V. Popov, Computational analysis of wind driven natural ventilation in buildings, Energy Build. 38 (5) (2006) 491–501.
[27] G.M. Stavrakakis, M.K. Koukou, M.G. Vrachopoulos, N.C. Markatos, Natural cross-ventilation in buildings: building-scale experiments, numerical simulation and thermal comfort evaluation, Energy Build. 40 (9) (2008) 1666–1681.
[28] S. Kato, S. Murakami, A. Mochida, S. Akabayashi, Y. Tominaga, Velocity-pressure field of cross ventilation with open windows analyzed by wind tunnel and numerical simulation, J. Wind Eng. Ind. Aerod. 44 (1–3) (1992) 2575–2586.
[29] I. Lee, S. Lee, G. Kim, J. Sung, S. Sung, Y. Yoon, PIV verification of greenhouse ventilation air flows to evaluate CFD accuracy, Trans. ASAE Am. Soc. Agric. Eng. 48 (2005) 2277–2288.
[30] S. Taddei, C. Manes, B. Ganapathisubramani, Characterisation of drag and wake properties of canopy patches immersed in turbulent boundary layers, J. Fluid Mech. 798 (2016) (2016) 27–49.
[31] C. Vanderwel, B. Ganapathisubramani, Effects of spanwise spacing on large-scale secondary flows in rough-wall turbulent boundary layers, J. Fluid Mech. 774 (2015) 1–12.
[32] A.G. Davenport, Rationale for determining design wind velocities, J. Struct. Div. Am. Soc. Civ. Eng. 86 (1960) 39–68.
[33] J. Wieringa, Updating the Davenport roughness classification, J. Wind Eng. Ind. Aerod. 41 (1–3) (1992) 357–368.
[34] A.K. Prasad, Particle image velocimetry, Curr. Sci. 79 (2000) 51–60.
[35] Y. Tominaga, A. Mochida, R. Yoshie, H. Kataoka, T. Nozu, M. Yoshikawa, T. Shirasawa, AIJ guidelines for practical applications of CFD to pedestrian wind environment around buildings, J. Wind Eng. Ind. Aerod. 96 (10–11) (2008) 1749–1761.
[36] J. Franke, A. Hellsten, H. Schlunzen, B. Carissimo, Best Practice Guideline for the CFD Simulation of Flows in the Urban Environment, COST Office, Brussels, 2007.
[37] B. Blocken, Computational Fluid Dynamics for urban physics: importance, scales, possibilities, limitations and ten tips and tricks towards accurate and reliable simulations, Build. Environ. 91 (2015) 219–245.
[38] B. Blocken, T. Stathopoulos, J. Carmeliet, CFD simulation of the atmospheric boundary layer: wall function problems, Atmos. Environ. 41 (2) (2007) 238–252.
[39] T. van Hooff, B. Blocken, Coupled urban wind flow and indoor natural ventilation modelling on a high-resolution grid: a case study for the Amsterdam ArenA stadium, Environ. Model. Softw 25 (1) (2010) 51–65.
[40] Q. Chen, Ventilation performance prediction for buildings: a method overview and recent applications, Build. Environ. 44 (4) (2009) 848–858.
[41] B. Blocken, 50 years of computational wind engineering: past, present and future, J. Wind Eng. Ind. Aerod. 129 (2014) 69–102.
[42] B. Blocken, LES over RANS in building simulation for outdoor and indoor applications : a foregone conclusion? Build. Simul. 11 (2018) 821–870.
[43] V. Yakhot, S.A. Orszag, S. Thangam, T.B. Gatski, C.G. Speziale, Development of turbulence models for shear flows by a double expansion technique, Phys. Fluids A Fluid Dyn. 4 (7) (1992) 1510–1520.
[44] D. Chodhury, Introduction to the Renormalization Group Method and Turbulence Modeling, (1993).
[45] F.R. Menter, Two-equation eddy-viscosity turbulence models for engineering applications, AIAA J. 32 (8) (1994) 1598–1605.
[46] D.C. Wilcox, Turbulence Modeling for CFD, DCW Industries, Inc., La Canada, California, 1998.
[47] ANSYS Inc, ANSYS Fluent Theory Guide vol. 15317, (2013), pp. 724–746.
[48] P.J. Roache, Qunatification of uncertainty in computational fluid dynamics, Annu. Rev. Fluid Mech. 29 (1) (1997) 123–160.
[49] H.B. Awbi, Ventilation of Buildings, Spon Press, London, New York, 2003.
[50] J.F. Michael Schatzmann, Helge Olesen, COST 732 Model Evaluation Case Studies : Approach and Results, (2010).
[51] E. Mundt, H.M. Mathisen, P. V Nielsen, A. Moser, REHVA Guidebook NO. 2:Ventilation Effectiveness, No. 2, Forssan Kirhapaino Oy, Forssa, Finland, 2004.
[52] J. Hang, Y. Li, Age of air and air exchange efficiency in high-rise urban areas and its link to pollutant dilution, Atmos. Environ. 45 (31) (2011) 5572–5585.
[53] T. van Hooff, B. Blocken, G.J.F. van Heijst, On the suitability of steady RANS CFD for forced mixing ventilation at transitional slot Reynolds numbers, Indoor Air 23 (3) (2013) 236–249.
[54] D. Etheridge, Natural Ventilation of Buildings: Theory, Measurement and Design, Chircester: John Wiley & Sons Ltd., United Kingdom, 2012.
[55] W.H. Snyder, Guideline for Fluid Modeling of Atmospheric Diffusion, US Environmental Protection Agency, 1981, p. 199 Report EPA-600/8-81-009.
[56] R.N. Meroney, Wind tunnel and numerical simulation of pollution dispersion: a hybrid approach, Paper for Invited Lecture at the Croucher, Advanced Study Institute, Hong Kong University of Science and Technology, 2004, pp. 6–10 December 2004.
[57] J. Neymark, R. Judkoff, G. Knabe, H.T. Le, M. During, A. Glass, G. Zweifel, Applying the building energy simulation test (BESTEST) diagnostic method to verification of space conditioning equipment models used in whole-building energy simulation programs, Energy Build. 34 (9) (2002) 917–931.